Title

Characterizing Cell-Specific Impacts of IRE1alpha-Mediated ER Stress Sensing in Obesity-Driven Metabolic Dysfunctions

Author

Li, Ruoyu

Publication Date

2023

Peer reviewed|Thesis/dissertation

Characterizing Cell-Specific Impacts of IRE1alpha-Mediated ER Stress Sensing in Obesity-Driven Metabolic Dysfunctions

By

Ruoyu Li

A dissertation submitted in partial satisfaction of the

requirements for the degree of

Doctor of Philosophy

in

Metabolic Biology

in the

Graduate Division

of the

University of California, Berkeley

Committee in charge:

Professor James Olzmann, Co-Chair
Professor Anders Näär, Co-Chair
Professor Jen-Chywan Wang
Professor Suneil Koliwad

Fall 2023

ABSTRACT

Characterizing Cell-Specific Impacts of IRE1alpha-Mediated ER Stress Sensing in Obesity-Driven Metabolic Dysfunctions
By

Ruoyu Li

Doctor of Philosophy in Metabolic Biology

University of California, Berkeley

Professor Suneil Koliwad, Chair

In mammalian cells and tissues, endoplasmic reticulum (ER) stress due to a disruption in the organelle's protein folding homeostasis is implicated in various metabolic diseases, notably obesity, type 2 diabetes (T2D), non-alcoholic fatty liver disease (NAFLD), and atherosclerosis. Inositol-requiring enzyme 1α (IRE1α), an ER-resident transmembrane protein, senses unfolded proteins, initiating the unfolded protein response (UPR) for adaptive transcriptional programs to restore ER balance. Additionally, IRE1α mediates inflammatory pathways, potentially driving the progression of metabolic impairments. Recent findings highlight IRE1α's ability to sense both unfolded-protein stress and lipid stress through distinct structural elements. Alleviating ER stress is considered protective against metabolic diseases, but the specific role of IRE1α, particularly in individual tissues or cell types, in driving metabolic disorders remains unexplored. This dissertation aims to 1) investigate IRE1α's role in metabolic dysfunctions, focusing on T2D, NAFLD, and atherosclerosis, and 2) generate IRE1α cell lines with specifically perturbed stress-sensing abilities.

Chapter 1 explores the impact of systemic IRE1α inhibition through both a small-molecule drug and genetic deletion of hepatic IRE1α in the context of T2D. The study demonstrates that both IRE1α inhibition and hepatocyte-specific deletion effectively prevent hyperglycemia and enhance hepatic insulin responsiveness. Transcriptional analysis of livers from both models identifies a set of downregulated genes associated with IRE1α inhibition/deletion, notably including those encoding for ER chaperones. Intriguingly, these genes, which are highly upregulated in obesity, are downregulated once more when IRE1α activity is blocked. This phenomenon, which we have termed "overchaperoning," is proposed as a potential cell-intrinsic mechanism driving insulin resistance.

Chapter 2 delves into the role of IRE1α in myeloid cells in mediating NAFLD pathogenesis. The studies demonstrate that the genetic deletion of IRE1α in myeloid cells effectively protects mice from NAFLD-associated steatosis and fibrosis. This observation suggests a mechanistic crosstalk between macrophages, hepatocytes, and hepatic stellate cells in the context of NAFLD.

Chapter 3 investigates the consequences of genetic IRE1α deletion in myeloid cells within the context of atherosclerosis. The findings indicate that myeloid-specific IRE1α deletion

led to reduced plaque expansion, plaque vascular smooth muscle cell (VSMC) content, and cellular proliferation in the aorta. These results suggest that IRE1α deletion in macrophages induces alterations in the vascular niche that ameliorate the progression of atherosclerosis in mice.

Chapter 4 focuses on genomic editing of IRE1α in a mouse macrophage cell line. Using a CRISPR-based approach, we successfully generated and validated an IRE1α functional knockout (KO) in an immortalized mouse macrophage cell line. In addition, we designed and validated the feasibility of the construct design for both a luminal domain deletion and a transmembrane domain mutation of IRE1 α, which were sufficient to disable induction of the UPR in response to unfolded protein accumulation vs. lipid excess, respectively.

TABLE OF CONTENTS

LIST OF FIGURES

LIST OF TABLES

ACKNOWLEDGEMENTS

I am profoundly grateful for the unwavering support and mentorship of Dr. Suneil Koliwad throughout my PhD journey. His belief in my potential, encouragement to explore, learn, and grow have been instrumental in shaping both my scientific and personal development. Without his guidance, I wouldn't be the scientist I am today. I also extend my gratitude to Dr. Martin Valdearcos Contreras, whose close guidance at the bench and encouragement in the face of challenges have been invaluable. Martin has exemplified what it means to be a dedicated scientist.

Special thanks to Dr. Feroz Papa and Dr. Luka Suzuki for their exceptional mentorship and guidance during our collaboration. Working with Luka has not only been professionally rewarding but has also brought joy to the collaborative process. I would also like to acknowledge Dr. Kevin Colón-Negrón for laying the foundation of our collaborative project and making significant contributions to the work presented in Chapter 1.

I express my profound gratitude to the members of my committee: Dr. Anders Näär, Dr. James Olzmann, and Dr. Jen-Chywan (Wally) Wang, for their brilliance and guidance throughout my journey. The enriching experiences from my rotations in James' and Wally's labs expanded my scientific horizon and formed invaluable friendships.

My lab mates played indispensable roles and have become lifelong friends. Special thanks to Stephen, Emily, Andrew, Diana, Moon Kyung, mama Annie, and Abby for their unwavering support. I also appreciate my volunteer student, Joachim Kavalakatt, now in medical school, for his contributions, enthusiasm for science, and for providing me with the opportunity to mentor.

Expressing heartfelt gratitude to Jerry, my husband, for always standing by my side and believing in me. My family and friends have been nothing but my strongest support in the face of difficulties. I would not be where I am today without them.

Lastly, I want to thank myself for never giving up and never forgetting who I am.

INTRODUCTION

ER Stress and Unfolded Protein Response

ER is a crucial organelle for proper protein folding and secretory protein synthesis. The accumulation of unfolded and misfolded proteins burdens the ER machinery, a condition known as ER stress. In metazoans, ER stress is sensed by three ER-residing transmembrane proteins: protein RNA-like ER kinase (PERK), activating transcription factor 6 (ATF6), and inositol-requiring enzyme 1alpha (IRE1α) [1–4]. The activation of these stress sensor proteins turns on an adaptive program, known as unfolded protein response (UPR), to restore ER homeostasis[5]. The adaptive UPR involves increased ER-associated protein degradation, ER chaperone synthesis, membrane lipid biosynthesis and repressed protein translation. These regulatory processes collectively alleviate the protein load and maintain ER function. In the face of chronic or irreversible ER stress, a terminal UPR will be triggered which induced cell death by activating apoptotic pathways[6]. For example, activation of PERK inhibits phosphorylation eukaryotic translation initiator factor 2α (eIF2α) to reduce translation but selectively increases induction of transcription factor 4 (ATF4), an activator of the C/EBP homologous protein(CHOP)-regulated apoptotic pathway[4].

While the UPR has traditionally been associated with protein stress, its broader significance has become increasingly evident. For example, the UPR is activated by cellular lipid excess as well as unfolded or misfold protein excess, a process termed "lipid stress" [7–9]. Moreover, elements of the UPR play crucial roles in diverse processes including lipid and cholesterol metabolism, energy homeostasis, and inflammation[10]. The intricate interplay between various stress signals and metabolic pathways relates to the molecular basis of these distinct stress-sensing components and their capacity to trigger a spectrum of UPR responses.

Inositol-Requiring Enzyme 1alpha (IRE1α)

IRE1α was initially characterized in *Saccharomyces cerevisiae* as the sole stress sensor regulating UPR and was found to be evolutionarily conserved across eukaryotes.[1] The protein structure of IRE1α typically includes three domains: the luminal domain (LD), transmembrane domain (TM), and cytosolic domain. The luminal domain is primarily responsible for sensing unfolded and misfolded proteins in ER lumen. The LD is normally bound by the ER chaperone protein BiP. Under ER stress, BiP binds to unfolded proteins instead, allowing IRE1α to form homodimers and activate downstream pathways[11–15]. Once dimerization occurs, the juxtaposed cytosolic kinase domains trans-autophosphorylate. This autophosphorylation event induces a conformational change and subsequently activates cytosolic RNase activity[16], which functions to cleave XBP1 mRNA at specific sites. The spliced form of XBP1 mRNA (sXbp1) encodes a critical transcription factor XBP1 that upregulates many genes involved in the adaptive UPR, including those for ER chaperones (Dnajb9, Dnajb11, Pdia3, and Dnajc3), ERAD machinery (Edem1, Herpud1, and Hrd1), and ER translocon (Sec61a1)[17–20]. Previous work from our lab showed that IRE1α's RNAse activity is required for NLR family pyrin

domain containing 3 (NLRP3) inflammasome activation and subsequent production of the pro-inflammatory cytokine interleukin-1 beta (IL-1β)[21].

Under chronic or irremediable stress, IRE1α dimers assemble into oligomers which trigger hyperphosphorylation of IRE1α[22]. The oligomeric form relaxes the specificity of the RNase activity of IRE1α, triggering splicing of many mRNA targets that share a splice site motif with Xbp1 mRNA. This process is known as the regulated IRE1α-dependent decay (RIDD)[23,24]. RIDD can result in apoptosis through the downregulation of mRNAs encoding key targets for protein folding, such as GRP78[24]. Additionally, the IRE1 kinase domain leads to apoptosis through ASK1/JNK signaling by inactivating anti-apoptotic BCL2 proteins[25].

Several studies have pointed out that IRE1α can also sense lipid stress through its TM domains[7–9]. Cho et al. showed that the human IRE1α TM domain exhibits a lipid-bilayer stress sensing function. Particularly, residues Ser450 and Trp457 are required for lipid stress induced IRE1α dimerization[8]. Notably, these non-canonical lipid-sensing functions are independent of the LD, which senses unfolded protein stress. Intriguingly, the early work from our lab also indicated that lipid-activation in macrophages induces a preferential transcription profile that was enriched in the adaptive but not terminal UPR genes[21]. Together, these studies provide evidence that protein-associated stress and lipid-associated stress are not only sensed by distinct structural elements but also induced by unique downstream cellular cascades.

CHAPTER 1

Pharmacological Targeting of IRE1α Ameliorates Insulin Resistance Through Preservation of the Hepatic Insulin Receptor Signaling Pathway

ABSTRACT

Type 2 diabetes (T2D) results from insulin resistance in metabolically responsive tissues (e.g. liver, muscle, and adipose), which ultimately leads to pancreatic β-cell dysfunction and impaired glycemic control. Obesity, a major T2D risk factor, induces ER stress in metabolic tissues, particularly in the liver, exacerbating insulin resistance. In this study, we demonstrated that in genetically-induced obese mice (ob/ob), IRE1α, a key component of the UPR, became hyperactivated during ER stress in insulin-responsive tissues. This hyperactivation desensitized the liver to insulin receptor signaling. Mice with hepatocyte-specific IRE1α deletion exhibited improved glucose tolerance in the context of diet-induced obesity. Additionally, we showed that specific inhibition of IRE1α with KIRA8, a potent and mono-selective kinase inhibitor, prevented the development of hepatic insulin resistance and improved glycemic control in obese mice. These findings suggest that IRE1α plays a role in the patho-etiology of insulin resistance in crucial metabolic cell types, and systemic targeting of IRE1α can modulate the UPR to enhance insulin sensitivity, thus mitigating obesity-induced diabetes.

INTRODUCTION

Diabetes incidents are projected to reach 693 million in 2045 due to the rising prevalence of obesity[26]. T2D, characterized by hyperglycemia and insulin resistance, accounts for approximately 90% of all diabetes[27,28].

Insulin resistance plays a pivotal role in the pathogenesis of T2D, with obesity being a major contributor. Visceral obesity, particularly associated with T2D risk, is often linked to other predictors of T2D, such as fatty liver disease and components of the metabolic syndrome. Studies highlight the significance of lipid accumulation and inflammation in metabolic tissues, especially the liver, as factors that may diminish the effectiveness of insulin-stimulated signaling, establishing a link between metabolically unhealthy obesity and insulin resistance[29]. Emerging data suggests that cellular stress experienced in the context of unhealthy obesity by metabolic cell types, such as adipocytes in white adipose tissues and hepatocytes in the liver, serves as a trigger for both tissue inflammation and associated insulin resistance. In investigating the drivers of such cellular stress, attention has been focused on ER stress, which activates an intracellular signaling pathway known as the UPR [30,31].

To date, IRE1α has been most extensively studied in type 1 diabetes (T1D) with the goal of preserving β-cell mass and function. Both *Ins-1* and *Ins-2* mRNA are reduced in β-cells under ER stress[32,33], and IRE1α deletion in NOD mice are protective from autoimmune destruction[34]. Moreover, our collaborating team led by Dr. Feroz Papa (UCSF) demonstrated that a class of small-molecule kinase inhibitors that prevent oligomerization of IRE1α to allosterically inhibit its RNase—Kinase Inhibitory RNase Attenuators (KIRAs)—is able to both prevent and reverse diabetes in the T1D NOD model[35]. Nevertheless, the mechanistic role of IRE1α in the development of antecedent insulin resistance in the context of T2D remained elusive.

We employed genetically modified *ob/ob* mice crossed into the BTBR background (BTBR*Lep*$^{ob/ob}$), previously characterized as an aggressive T2D mouse model by Clee et al. Theses mice develop hyperglycemia and hyperinsulimia as early as 6 week of age[36]. Our study aimed to investigate the impact of systemic IRE1α inhibition through administration of KIRA8, a mono-selective and potent IRE1α inhibitor[37,38]. Additionally, we explored how hepatocyte-specific IRE1α inhibition could prevent hyperglycemia. To understand the underlying mechanisms of how IRE1α contributes to T2D, we performed RNAseq analysis on liver samples from mice with systemic and hepatocyte-specific IRE1α perturbation.

RESULTS

IRE1α Inhibition by KIRA8 Protects Btbr*lep*$^{ob/Ob}$ Mice Against Obesity-Induced Hyperglycemia

The preliminary data from the Papa lab provided the foundation for understanding the impact of IRE1α on systemic glycemic control[39]. We hypothesized that KIRA8 might be effective in preventing T2D-like manifestations in BTBR*Lep*$^{ob/ob}$ mice through inhibition of IRE1α activity in metabolic tissues. 4-week old BTBR*Lep*$^{ob/ob}$ mouse cohorts were treated with 50mg/kg of KIRA8 intraperitoneally (IP) for 5 days a week for 3 weeks. The BTBR*Lep*$^{ob/ob}$ mice develop insulin resistance by 4 weeks of age and become hyperglycemia by 6 weeks of age[40]. However, Colon-Negron et. al. found that BTBR*Lep*$^{ob/ob}$ mice treated with KIRA8 maintained normal random blood glucose levels throughout treatment periods compared to vehicle-treated mice (519.6 ± 36.6 mg/dL for vehicle-treated BTBR$^{Lepob/ob}$ mice and 208.9 ± 12.7 mg/dL for KIRA8-treated BTBR$^{Lepob/ob}$; $p < 0.0001$) (**Figure 1.1A**). In addition, Colon-Negron et. al. performed glucose tolerance test (GTT) with IP glucose (2g/kg) and found that the KIRA8-treated group had improved glucose disposal compared to that of vehicle-treated group (**Figure 1.1B**). These findings indicated that KIRA8 treatment is sufficient to prevent glucose intolerance driven by obesity.

KIRA8-treated BTBR$^{Lepob/ob}$ mice were also associated with a significant reduction in body weight gain over time when compared to the vehicle-treated group (**Figure 1.1C**). Therefore, we sought to rule out the possibility that the glucose improvements were due to reduced weight gain by strategically altering the KIRA8 dosing formulation — switching from dissolving KIRA8 in a tween/ethanol vehicle to a commercially available solvent (sulfonyl ether7 β-cyclodextrin; Captisol by Ligand Pharmaceuticals)[41]. In order to reduce high-dose toxicity, we injected mice twice a day with total loading dose of 100mg/kg per day for 2 weeks starting at 3 weeks of age, followed by 4 weeks of twice-a-day injection at 50mg/kg per day. With this new formation and dosing regimen, we found that the KIRA8 treatment no longer drove body weight gain when compared to the Captisol-vehicle group (**Figure 1.1F**). Remarkably, KIRA8/Captisol-treated BTBR$^{Lepob/ob}$ mice still displayed lower random glucose levels and improved glucose disposal as measured by GTT (**Figure 1.1D&E**). These findings indicate that the previously observed body weight reduction is formulation-dependent, excluding the possibility that the previous glucose improvements were due to reduced weight gain or differential food

intake. In summary, systemic KIRA8-inhibition of IRE1α preserved glucose homeostasis independent of factors that are involved in regulating energy balance.

KIRA8 Ameliorates Systemic Insulin Resistance and Hepatic Gluconeogenesis

To explore the mechanism by which Inhibiting IRE1α preserves glycemic control in BTBR*Lep*$^{ob/ob}$ mice, we next examined the effect of KIRA8 on systemic insulin responsiveness. We first noticed that the fasting insulin level of the KIRA8-treated mice was two-fold lower than that of the vehicle-treated mice (**Figure 1.1G**). Moreover, the insulin tolerance test (ITT) (2IU/kg) showed that KIRA8-treated BTBR*Lep*$^{ob/ob}$ mice were significantly more insulin tolerant than the vehicle-treated animals (**Figure 1.1H**). This data was further corroborated by the Homeostatic Model Assessment for Insulin Resistance (HOMA-IR), an established index of insulin sensitivity[42], with KIRA8-treated BTBR*Lep*$^{ob/ob}$ group (HOMA-IR of 57.3 ± 15.5) presenting with greater insulin sensitivity than that of the vehicle-treated group (HOMA-IR of 304.1 ± 56.8) (**Figure 1.1I**).

Insulin resistance is often accompanied by dyslipidemia, which involves increased level of circulating very low-density lipoproteins (VLDLs) and triglyceride-rich particles[43]. We found a significantly reduced fasted, circulating TG level when sampling the plasma of KIRA8-treated animals compared to that of vehicle-treated mice (**Figure 1.1J**). In individuals with high insulin levels, hepatic gluconeogenesis (GNG) is constitutively high[44–48]. Therefore, we next measured the fasting ketone body level in circulation and found that KIRA8 treatment significantly reduced the levels of β-hydroxybutyrate compared to that of the vehicle-treated control (**Figure 1.1K**). In late post-prandial hepatic GNG, pyruvate is used as a substrate. A high glycemic area-under-the-curve (AUC) in a pyruvate tolerance test (PTT) is an indicator of compromised hepatic insulin responsiveness. Therefore, we examined the impact of KIRA8 treatment on the glycemic excursion of BTBR*Lep*$^{ob/ob}$ mice through the PTT. The BTBR*Lep*$^{ob/ob}$ animals exhibited a robust glycemic excursion, in line with the insulin-resistant phenotype. Notably, KIRA8 treatment completely abrogated the elevated glycemic response to pyruvate injection, indicating these mice had preserved hepatic insulin responsiveness (**Figure 1.1L**). In addition, we further validated our findings with GNG-related gene expression analysis. The transcriptional levels of the genes encoding phosphoenolpyruvate carboxykinase (*Pck1*) and glucose 6-phosphatase (*G6pc*) were significantly elevated in the liver of BTBR*Lep*$^{ob/ob}$ mice when compared to that of the BTBR*Lep*^{WT} controls (**Figure 1.1M**). However, KIRA8 significantly mitigated these increases (**Figure 1.1M**), substantiating our finding that KIRA8 is sufficient for sensitizing hepatic insulin response.

KIRA8 Restores Insulin Signaling in Metabolic Tissues

Given that KIRA8 restored systemic insulin sensitivity, we next explored whether KIRA8 could similarly restore insulin signaling in metabolic tissues in the obesity context. First, we assessed cellular phosphorylation (Ser473) of AKT, a key step in the insulin receptor signaling pathway, in the liver of BTBR*Lep*$^{ob/ob}$ mice. We found that p-AKT levels were blunted in response to insulin administration in the liver samples collected from vehicle-treated BTBR*Lep*$^{ob/ob}$ mice; however, KIRA8 treatment profoundly increased p-AKT levels, supporting our previous findings on KIRA8's ability to potentiate hepatic insulin

responsiveness (**Figure 1.2A**). Likewise, in the adipose tissue, KIRA8 was able to rescue p-AKT levels in response to insulin administration (**Figure 1.2B**). Together, these results demonstrate that systemic KIRA8 treatment can normalize insulin signaling, which is otherwise impaired, in major metabolic tissues.

KIRA8 Rescues Insulin Signaling in Unfolded Protein- and Palmitate-Challenged Hepatic Immortalized Cell Lines

To confirm our findings that KIRA8 treatment could effectively sensitize insulin responsiveness in liver, we assessed insulin signaling pathway under different ER stress-challenged conditions in immortalized liver cell lines. We pretreated both HepG2 (human hepatocyte cell line) and H4IIEC3 (rat hepatocyte cell line) with KIRA8 for 1 hour prior to administration of Tunicamycin (Tm, an unfolded protein inducer) and palmitic acid (PA, a type of saturated fatty acid) respectively. First, we confirmed the on-target effect of KIRA8 by demonstrating that KIRA8 pre-treatment effectively blocks Tm- and PA-induced Xbp1 splicing (**Figure 1.2C & D**). Notably, KIRA8 restored insulin-induced p-AKT levels that were significantly blunted in both of Tm-treated (25ng/ml and 50ng/ml) HepG2 cells and PA-treated (100uM) H4IIEC3 cells (**Figure 1.2E & F**). Taken together, these findings indicate that IRE1α is critical for the mechanism by which ER stress disrupts insulin receptor signaling and that blocking the functions of IRE1α is sufficient for rescuing insulin signaling in stress-challenged liver cells.

Hepatocyte-Specific lRE1α-Deficient Mice Show Suppression of ER stress Signaling and Amelioration of Diet-Induced Glucose Intolerance

Given the strong evidence that systemic IRE1α inhibition improves insulin responsiveness, potentially contributing to improved glycemic control, we next examined whether genetically deleting IRE1α in the liver could rectify diet-induced impairment of glycemic control in mice.

We generated a hepatocyte-specific IRE1α deletion mouse model (IRE1α-LivKO) by crossing a mouse line expressing floxed (exon 16 and 17) alleles of *Ern1* (gene name of IRE1α) (courtesy of Dr. Randal Kaufman, Sanford-Burnham Research Inst.) with mice expressing Cre recombinase under the control of a hepatocyte-specific promoter (*Alb*-Cre). IRE1α $^{f/f}$ littermates (WT) that were not crossed with *Alb-Cre* mice served as the control group (**Figure 1.3A**).

We first validate the KO efficiency by performing qRT-PCR and immunoblotting of liver tissues obtained from chow-fed IRE1α-LivKO or WT mice. The gene expression of IRE1α was reduced by more than 90% in the liver of IRE1α-LivKO compared to that of WT (**Figure 1.3B**). KO efficiency was also confirmed through immunoblotting of liver tissues: WT samples clearly expressed full-length IRE1α protein, while IRE1α-LivKO samples expressed only lower molecular weight bands (presumably truncated mutant protein) with nearly a complete absence of full-length WT protein (**Figure 1.3C**).

In addition, we also performed an *in vivo* acute pharmacodynamic study to confirm that IRE1α was functionally knocked out. Both chow-fed IRE1α-LivKO and WT mice were

fasted for 8 hours and IP-injected with Tm or vehicle at the beginning of the last 4 hours of fasting. We found that Tm induced robust Xbp1 splicing in the liver of WT mice. However, this effect was ablated in the liver of IRE1α -LivKO mice (**Figure 1.3D & E**). Furthermore, IRE1α gene expression in WT mice was increased by more than 3-fold in response to Tm induction, whereas no changes were observed in the livers of IRE1α -LivKO animals (**Figure 1.3F**). *Erdj4*, a downstream target of the XBP1 transcription factor, was upregulated in WT livers by almost 10-fold following Tm administration but was unchanged in IRE1α-LivKO samples (**Figure 1.3G**). Lastly, gene expression of *Blos1*, one of the RIDD targets, was significantly decreased in the liver by Tm administration in WT but remained unchanged in the IRE1α-LivKO livers following Tm administration (**Figure 1.3H**). Overall, these results validated the efficiency of IRE1α knockdown in the livers of IRE1α-LivKO mice.

To develop insulin resistance, IRE1α-LivKO and WT mice were put on "western-type" high-fat diet (HFD) for total 10 weeks. Notably, IRE1α-LivKO mice had significantly improved glucose tolerance when compared to WT group (**Figure 1.3I**). Although IRE1α-LivKO and WT mice presented comparable levels of systemic insulin resistance as measured by ITT (**Figure 1.3J**), the PTT showed that IRE1α-LivKO mice possessed significantly higher hepatic insulin responsiveness than that of WT animals (**Figure 1.3K**). These results suggest that IRE1α deletion in the liver improved glycemic control and hepatic insulin responsiveness, but the deletion was insufficient for rescuing systemic insulin resistance, ultimately implying that IRE1α inhibition in other metabolic tissues might be involved in the enhancement of that process.

Inactivation of IRE1α Results in Decreased Expression of ER Stress-Related Genes

To understand the mechanisms by which systemic IRE1α inhibition restore hepatic insulin sensitivity, we analyzed mRNA isolated from the livers of BTBR*Lep*$^{ob/ob}$ mice treated with KIRA8 (50 mg/kg) for 5 weeks versus those of mice treated with vehicle starting at 4 weeks of age. RT-qPCR revealed that ER stress-associated genes encoding for ATF4, XBP1, CHOP, and BiP were significantly upregulated in the vehicle-treated BTBR*Lep*$^{ob/ob}$ mice compared to BTBR^{WT} controls, but this effect was robustly reversed with KIRA8 treatment (**Figure 1.4A**). Surprisingly, the expression of BiP, which functions to alleviated ER stress and is positively associated with glycemic protection in both human and mouse studies[49–51], was upregulated in the most insulin-resistant group. This unexpected result prompted us to perform unbiased transcriptional profiling of RNA isolated from BTBR*Lep*$^{ob/ob}$ mice.

The RNA-seq results revealed that KIRA8 treatment induced an overall change in the transcriptional signature within the livers of BTBR*Lep*$^{ob/ob}$ mice when compared to those of vehicle-treated mice (**Figure 1.4B**), and sets of differentially expressed genes (DEGs) were identified (**Figure 1.4C**). Through gene ontology (GO) analysis of upregulated and downregulated genes following KIRA8 treatment, we found an enrichment of genes encoding proteins involved in ER protein folding, ER chaperones, UPR, and ubiquitin-dependent ER-associated degradation (**Figure 1.4D**). Specifically, numbers of these mRNA were downregulated by KIRA8 treatment (**Figure 1.4E**).

In parallel, we performed RNA-seq analysis on RNA isolated from the livers of IRE1α-LivKO and control mice on HFD. While the overall transcriptional pattern was distinct from that in the livers of BTBR*Lep*$^{ob/ob}$ mice (**Figure 1.4F & G**), we observed profound similarities when viewing the DEGs in GO and KEGG analyses. Both approaches revealed, in the genes downregulated by IRE1α hepatic KO, an enrichment of pathways involved in "protein transport" and "protein process in ER" (**Figure 1.4H**). However, the effect size was smaller than the changes observed in the KIRA8-treated BTBR*Lep*$^{ob/ob}$ livers.

In summary, we observed that both systemic IRE1α inhibition with KIRA8 and genetic hepatocyte-specific IRE1α KO yields clusters of genes that were downregulated by IRE1α perturbation. More specifically, these clusters were enriched in genes involved in ER protein folding pathways, particularly those encoding for chaperone proteins. Chaperones are generally considered to be protective, but these chaperones were highly expressed in the insulin-resistant BTBR*Lep*$^{ob/ob}$ livers, which could be a result of excessive compensation to the metabolic challenge.

DISCUSSION

In the study above, we showed that pharmacological IRE1α inhibition using small molecule drug KIRA8 improves glycemic control (via GTT), systemic insulin resistance (via ITT), and hepatic insulin responsiveness (via PTT). These results were further validated in the genetically engineered hepatocyte-specific IRE1α deficient mice which were glucose- and pyruvate-tolerant, indicating that blocking IRE1α enhances liver-intrinsic insulin responsiveness. In addition, our *in vitro* experiments using ER stress-challenged immortalized liver cell lines also suggested that IRE1α exerts cell-autonomous disruption of insulin-receptor signaling.

Our RNA-seq analysis on two independent mouse models revealed that lacking IRE1α activity yields a reduction in the mRNAs of specific ER stress-related genes in the liver. Paradoxically, we observed abnormally high levels chaperone BiP in the insulin-resistant mice, the expression of which is generally associated with improved glycemic state[49–52]. This "over-chaperoning" phenomenon has been studied in many other works in which "over-chaperoning" can be detrimental for proper metabolic capacity by inducing excessive protein folding and aberrant modifications of catalytic activities[53–55]. For example, in *Drosophila*, the overexpression of chaperone Hsp70 hinders proper cell growth and development[56,57]. Similar deleterious effects of "over-chaperoning" has been observed in mammalian cancer models[58,59]. We suspect that KIRA8 and liver-specific IRE1α deficiency may be restoring healthy ER protein processing by reducing chaperone levels.

The series of experiments conducted in this investigation have successfully elucidated the underlying mechanisms of UPR-induced insulin resistance in physiologically relevant murine models of T2D[30,60,61]. Our findings shed light on the potential of targeting the IRE1α axis using KIRA8, demonstrating the drug's capacity to restore impaired insulin signaling during ER stress. This intervention resulted in increased

insulin sensitivity, suggesting a potential strategy for the prevention or reversal of T2D. Noteworthy upstream modulators of XBP1, such as TUDCA and IXA4, have been previously reported for mitigating insulin resistance[30,61]. However, KIRA8, distinguished as a selective ON-target tool, presents an avenue for further advancement. Future work to optimize KIRA8 and similar pharmacophores for targeting IRE1α may yield pre-clinical candidates with potential for disease modification in metabolic tissues.

MATERIALS AND METHODS

Mouse Studies

Male BTBR*Lep*$^{ob/ob}$ mice [BTBR.Cg-*Lep*^{ob}/WiscJ] , Albumin-Cre (Alb-Cre) mice [B6.Cg-*Speer6-ps1*$^{Tg(Alb-cre)21Mgn}$*/J*, hepatocyte specific recombination], and C57BL/6J mice were obtained from Jackson Laboratories (stock numbers: 004824, 035593, and 000664, respectively). BTBR*Lep*$^{ob/ob}$ mice were genotyped by following the instruction of Jackson Laboratories. To generate diet induced obesity, C57BL/6J & Alb-Cre mice were fed a "western-type" high fat diet (HFD) with 42% kcal from fat (milkfat), plus elevated cholesterol and sucrose content (Envigo; TD.88137), for 10 weeks starting at 6-8 weeks of age. Blood glucose levels were measured from tail snips obtained between 8:00 AM and 10:00 AM using a LifeScan glucometer (OneTouch Ultra) twice per week. All procedures were performed in accordance with protocols approved by the Institutional Animal Care and Use Committee at the University of California, San Francisco. Animals were kept in a specific pathogen-free animal facility on a 12 hr light- dark cycle at an ambient temperature of 21°C. They were given free access to water and food.

Synthesis of KIRA8

*(S)-2-chloro-N-(6-methyl-5-((3-(2-(piperidin-3-ylamino)pyrimidin-4-yl)pyridin-2 yl)oxy)naphthalen-1-yl)benzenesulfonamide (KIRA8):*A solution of (S)-tert-butyl 3-((4-(2-((5-(2-chlorophenylsulfonamido)-2-methylnaphthalen-1-yl)oxy)pyridin-3-yl)pyrimidin-2-yl)amino) piperidine-1-carboxylate (4.36 g, 6.22 mmol) in DCM (15 ml) was treated with HCl in dioxane (3.5 M, 4 ml) and stirred at 50°C for 1 hr. The solution was then concentrated, and the remaining solid was triturated with Et_2O. Drying over P_2O_5 in a vacuum desiccator gave (S)-2-chloro-N-(6-methyl-5-((3-(2- (piperidin-3-ylamino)pyrimidin-4-yl)pyridin-2-yl)oxy)naphthalen-1-yl)benzenesulfonamide as an off-color and free-flowing solid (3.56 g, 90%). Product was determined to be 97.4% pure by reverse phase analytical chromatography (HPLC). ESI-MS: m/z = 601.3 $[M+H]^+$ (consistent with previously described characterization. Compound #18 in Harrington et al., 2014).

KIRA8 Treatments in Genetically Obese BTBR*Lep*$^{ob/ob}$ Mice and Diet Induced Obese Mice

Male BTBR*Lep*$^{ob/ob}$ mice were randomized to KIRA8 or vehicle groups, and injected I.P. with KIRA8 (50 mg/kg) or vehicle (3% ethanol: 7% Tween-80: 90% saline) once a day, 5 times a week. 4-week-old BTBR*Lep*$^{ob/ob}$ mice were used for the first protocol of the prevention studies. For the new formulations, we used ether7 β-cyclodextrin (Captisol). Also, we changed the regimen of dosing from once a day 50 mg/kg of KIRA8 for entire treatment period to 2 weeks of loading dose with 100 mg/kg divided to two dosing/day

(morning and evening) followed by 50 mg/kg for maintenance dosing also divided to two dosing/day for another 3 weeks. Mice that were euthanized due to complication attributed to overt diabetes were excluded from the final analysis. In reversal studies, obesity was first established in C57BL/6J mice with 10 weeks of HFD. At week 11 of HFD, KIRA8 (20 mg/dl) or vehicle treatment was administered I.P. 5 times a week for 4 weeks, while mice were maintained on HFD. Blood glucose and body weight were monitored twice weekly.

Glucose, Insulin, and Pyruvate Tolerance Tests

BTBR*Lep*$^{ob/ob}$ mice were fasted for 6 hr before I.P. injection with glucose (2g/kg), insulin (2IU/kg), or pyruvate (2g/kg). IRE1α-LivKO and WT control mice were fasted for 6 hours before I.P. injection with glucose (2g/kg) or pyruvate (2g/kg) and fasted for 4 hours before injection with insulin (0.5IU/kg). Blood was collected from the tail vein after an initial small tail clip, and glucose levels were determined using LifeScan glucose meter (OneTouch Ultra). Concentrations of reagents are specified in figure legends.

RNA Isolation, Quantitative Real-time PCR, and Primers

RNA was isolated from tissue using TRIzol (Invitrogen). Up to 1 μg total RNA was reverse transcribed into cDNA using the QuantiTect Reverse Transcription Kit (QIAGEN). Differences in relative gene expression were quantified by qRT-PCR using SYBR Green (QIAGEN) and StepOnePlus Real-Time PCR System (Applied Biosystems). Thermal cycles were: 5 min at 95°C, 40 cycles of 15 s at 95°C, 30 s at 60°C. Gene expression levels were normalized to 18S rRNA housekeeping gene. Sequences of primers used for qPCR can be found in Table 1.

Insulin, Triglycerides, and Ketones Determination

All measurements were performed after fasting animals for 6 hrs. Serum insulin levels were detected by ELISA following manufacturer instructions (EMD Millipore; Cat. #: EZRMI-13K). Triglycerides and ketones were measured using a commercial kit from Sigma (Cat. #: TR0100-1KT and MAK134-1KT).

Tissue Culture

HepG2 cells (human hepatocyte cell line), H4IIEC3 cells (rat hepatocyte cell line), and HEK293 T-REx cells (human embryonic kidney cell line) were grown and maintained in Dulbecco's Modified Eagle Media (DMEM) containing 5 mM glucose. DMEM was supplemented with 10% heat-inactivated fetal bovine serum (FBS, J.R. Scientific), 100U penicillin, and 100U streptomycin. Specifically, 1 mM sodium pyruvate and 10 mM HEPES was added to DMEM for H4IIEC3 cells. For starvation, cells were maintained in FBS-free media for the indicated times in their respective experiments.

Western Blots and Antibodies

For protein analysis, cells were lysed in M-PER buffer (Thermo Scientific) or T-PER buffer for ~100 mg of mouse tissue plus complete EDTA-free protease inhibitor and phosphatase inhibitor (Roche). Protein concentration was determined using Rapid Gold BCA Protein Assay (Thermo). Western blots were performed using 4%–12% Bis-Tris (NuPage). Gels were migrated using MES buffer and transferred onto nitrocellulose transfer membrane using an iBlot 2 Dry Blotting System (Themro). Antibody binding was

detected with near-infrared- dye-conjugated secondary antibodies (LI-COR) on the LI-COR Odyssey scanner. Blocking, antibody incubation, and washing were done in TBS with 0.05% Tween-20 (v/v). Band intensities were quantified by densitometry using ImageJ (NIH). GAPDH and Actin were used as loading controls. Antibodies and respective dilutions are listed in Table 2.

XBP1 mRNA Splicing

RNA was isolated from tissues and reverse transcribed as above to obtain total cDNA. Then, XBP1 primers were used to amplify an XBP-1 amplicon spanning the 26 nt intron from the cDNA samples in a regular 3-step PCR. Thermal cycles were: 5 min at 95°C, 30 cycles of 30 sec at 95°C, 30 sec at 60°C, and 1 min at 72°C, followed by 72°C for 15 min, and hold at 4°C. Primers used for XBP1 mRNA splicing were as follows: human sense primer (5′- GTATCTCTAAGACTAGGGGCTTGG -3′), human antisense primer (5′- AAACAGAGTAGCAGCTCAGACTGC -3′), rat sense primer (5′- AGGAAACTGAAAAACAGAGTAGCAGC-3′), and rat antisense primer (5′- TCCTTCTGGGTAGACCTCTGG -3′). PCR fragments were then digested by PstI, resolved on 3% agarose gels, stained with EtBr and quantified by densitometry using ImageJ (NIH).

AKT Ser473 Determination Assay

HepG2 and H4IIEC3 cells were pretreated with KIRA8 for 1 hour prior to treatment with ER stress agents. Later, Tunicamycin (EMD Millipore), Brefeldin A (Sigma), or Palmitate (Nu-Check Prep) was added to the media and cells were incubated at 37°C in FBS-free media. After 24 hours, insulin at the specified concentration was added to the media and cells were incubated for 5 minutes. AKT Ser 473 phosphorylation was then analyzed by western blot. For T-Rex293 cells, they were pretreated with KIRA8 for 1 hour before administration of Dox. Cells were then co-treated with KIRA8 and Dox (1 µg/mL) for 48 hours, incubated for the last 24 hours in FBS-free media. After 48 hours, AKT Ser473 phosphorylation was stimulated upon addition of 10 nM of insulin for 5 minutes and determined through western blot.

Statistical Analysis

All statistical analyses were performed using GraphPad Prism version 8.1 software. Student's t test or two-way ANOVA were applied to determine statistical difference between two groups. Data are presented as mean ± SEM. Significance was defined by a p value < 0.05. p values: * < 0.05; ** < 0.01; *** < 0.001; N.S., non-significant.

TABLE 1.1 List of primers used for qPCR in mouse livers

Gene	Forward Primer	Reverse Primer
PEPCK	GTCACCATCACTTCCTGGAAGA	GGTGCAGAATCGCGAGTTG
G6P	AGGTCGTGGCTGGAGTCTTGTC	GTAGCAGGTAGAATCCAAGCG
18s	GTAACCCGTTGAACCCCATT	CCATCCAATCGGTAGTAGGC

TABLE 1.2 List of antibodies used for western blot

Antibody	Source (Catalog number)	Dilution
p-c-Jun	CST (# 9164)	1:1000
total c-Jun	CST (# 9165)	1:1000
XBP1	Proteintech (# 25997-1-AP)	1:1000
BiP	CST (# 3177)	1:1000
p-IRE1α Ser724	Novus Biologicals (# NB100-2323)	1:500
total IRE1α	CST (# 3294)	1:1000
Myc	Santa Cruz Biotechnology (# sc-40)	1:1000
p-AKT Ser473	CST (# 9271)	1:1000
total AKT	CST (# 9272)	1:1000
Actin	Santa Cruz Biotechnology (# sc-47778)	1:2000
GAPDH	CST (# 2118)	1:2000

TABLE 1.3 List of primers used for qPCR to determine UPR markers in mouse livers

Gene	Forward Primer	Reverse Primer
ATF4	GCAAGGAGGATGCCTTTTC	GTTTCCAGGTCATCCATTCG
XBP1	CCGTGAGTTTTCTCCCGTAA	AGAAAGAAAGCCCGGATGAG
CHOP	CTCCAGATTCCAGTCAGAGTTC	CCACTCTGTTTCCGTTTCCTA
BIP	GCATATGGCCTGGATAAGAGAG	GTCAATGGTGAGAAGAGACACA
18s	GTAACCCGTTGAACCCCATT	CCATCCAATCGGTAGTAGGC

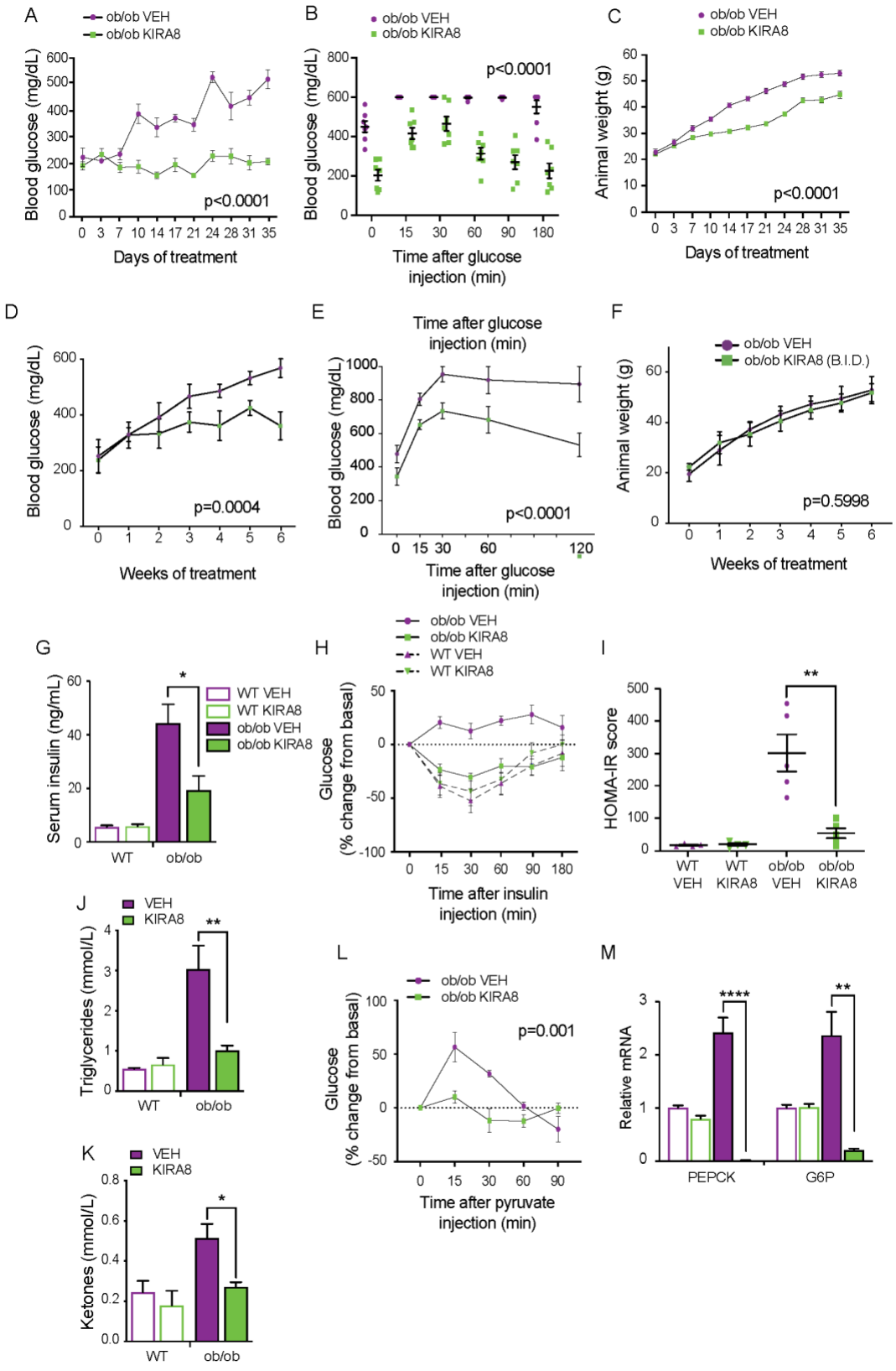
A
ob/ob VEH
ob/ob KIRA8
Blood glucose (mg/dL)
p<0.0001
Days of treatment
B
ob/ob VEH
ob/ob KIRA8
Blood glucose (mg/dL)
p<0.0001
Time after glucose injection (min)
C
ob/ob VEH
ob/ob KIRA8
Animal weight (g)
p<0.0001
Days of treatment
D
Blood glucose (mg/dL)
p=0.0004
Weeks of treatment
E
Time after glucose injection (min)
Blood glucose (mg/dL)
p<0.0001
Time after glucose injection (min)
F
ob/ob VEH
ob/ob KIRA8 (B.I.D.)
Animal weight (g)
p=0.5998
Weeks of treatment
G
Serum insulin (ng/mL)
WT VEH
WT KIRA8
ob/ob VEH
ob/ob KIRA8
WT
ob/ob
H
ob/ob VEH
ob/ob KIRA8
WT VEH
WT KIRA8
Glucose (% change from basal)
Time after insulin injection (min)
I
HOMA-IR score
WT VEH
WT KIRA8
ob/ob VEH
ob/ob KIRA8
J
VEH
KIRA8
Triglycerides (mmol/L)
WT
ob/ob
K
VEH
KIRA8
Ketones (mmol/L)
WT
ob/ob
L
ob/ob VEH
ob/ob KIRA8
p=0.001
Glucose (% change from basal)
Time after pyruvate injection (min)
M
Relative mRNA
PEPCK
G6P

FIGURE 1.1 KIRA8 treatment prevents hyperglycemia and improves blood glucose disposal by enhancing insulin responsiveness in the BTBR*Lep*$^{ob/ob}$ mice.

A) Random morning (AM) blood glucose (BG) levels in male BTBR*Lep*$^{ob/ob}$ mice I.P. injected for 35 days once a day with KIRA8 (50 mg/kg) (n = 7) or vehicle (n = 7) starting at day 28 of age. BGs (mean ± SEM), analyzed by two-way RM ANOVA; $p < 0.0001$. **B)** Glucose Tolerance Tests (GTT) on day 28 post injections. Male BTBR*Lep*$^{ob/ob}$ mice were fasted for 6 hours then I.P. injected with a glucose (2g/kg) (KIRA8 n = 7, vehicle n = 7). Each square shape represents an individual mouse. Two-way RM ANOVA; $p < 0.0001$. **C)** Body weights of BTBR*Lep*$^{ob/ob}$ mice. Two-way RM ANOVA; $p < 0.0001$ (BTBR*Lep*$^{ob/ob}$) and $p < 0.0001$ (WT). **D)** Random AM BG levels in male BTBR*Lep*$^{ob/ob}$ mice with Captisol formulation on B.I.D. protocol. Mice were injected for 14 days twice a day of KIRA8 with the dose of 100 mg/kg in total followed by 28 days of treatment with half the dose (50mg/kg in total) (n = 7) or vehicle (n = 7) starting at day 21 of age. BGs (mean ± SEM). **(E)** Glucose Tolerance Tests (GTT) on 5 weeks post injections with B.I.D. KIRA8 on male BTBR*Lep*$^{ob/ob}$ mice that were fasted for 6 hours then I.P. injected with a glucose (2g/kg) (KIRA8 n = 7, vehicle n = 4). Two-way RM ANOVA; $p < 0.0001$. **F)** Body weights of male BTBR*Lep*$^{ob/ob}$ I.P. injected KIRA8 with Captisol formulation on B.I.D. protocol. Mice were injected for 14 days twice a day of KIRA8 with the dose of 100 mg/kg in total followed by 28 days of treatment with half the dose (50mg/kg in total) (n = 7) or vehicle (n = 7) starting at day 21 of age. **G)** Insulin levels in WT and BTBR*Lep*$^{ob/ob}$ mice on day 56 (28 days post-injection) measured. **H)** Insulin (2 IU/kg) tolerance tests were performed on day 56 (28 days post injections) in WT and BTBR*Lep*$^{ob/ob}$ mice after fasted for 6 hours. Data are represented as the percent of change from the basal blood glucose levels at 0 min (KIRA8 n = 5 and vehicle n = 4 – 5). Two-way RM ANOVA; $p < 0.0037$. **I)** Homeostatic Model Assessment index for Insulin Resistance (HOMA-IRA) in WT and BTBR*Lep*$^{ob/ob}$ mice at day 56 (28 days post injections). Values were calculated using the equation $(G_0 \times I_0)/405$, where G_0 and I_0 are the fasting basal glucose and insulin levels, respectively (n= 4 – 5 animals in each group). Each symbol denotes an individual mouse. **J & K)** Triglycerides (J), and Ketones (K) levels in blood collected from 6 hours fasted WT BTBR and BTBR*Lep*$^{ob/ob}$ mice 35 days after treatment. (KIRA8 n = 5 and vehicle n = 4 – 5). **L)** Pyruvate Tolerance Tests (PTT) on day 56 (28 days post injections) of 6 hours fasted BTBR*Lep*$^{ob/ob}$ mice after challenged with 2 g/kg sodium pyruvate (KIRA8 n = 3, vehicle n = 4). Two-way RM ANOVA; $p < 0.0010$. **M)** Expression of gluconeogenic genes in liver of WT and BTBR*Lep*$^{ob/ob}$ mice 28 days post injections was measured by quantitative real-time PCR with 18S ribosomal mRNA as control. Bars represent means ± SEM. p values: * < 0.05, ** < 0.01, *** < 0.001, **** < 0.0001.

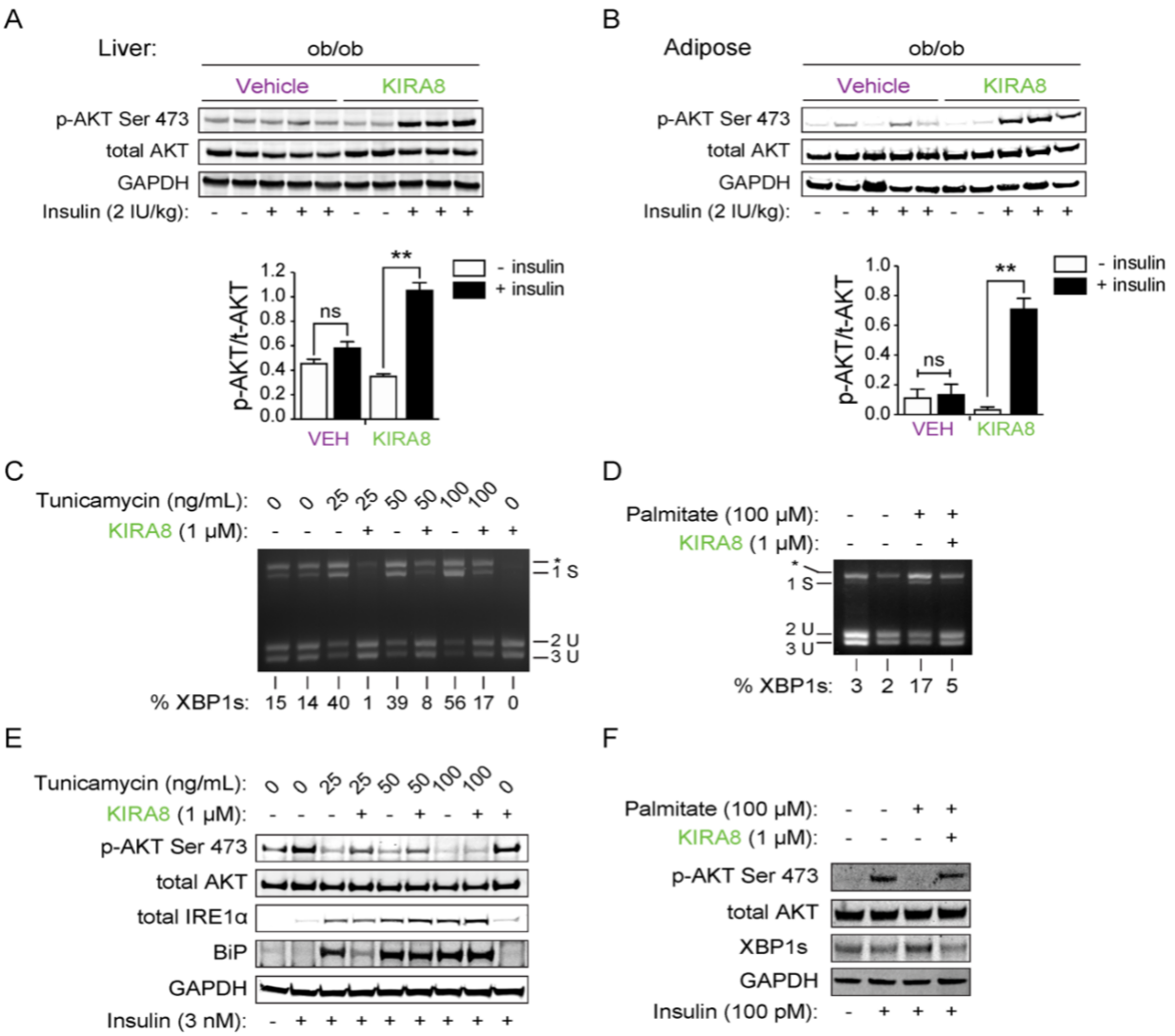
A
Liver:
ob/ob
Vehicle
KIRA8
p-AKT Ser 473
total AKT
GAPDH
Insulin (2 IU/kg): - - + + + - - + + +
p-AKT/t-AKT
ns
**
- insulin
+ insulin
VEH
KIRA8
B
Adipose
ob/ob
Vehicle
KIRA8
p-AKT Ser 473
total AKT
GAPDH
Insulin (2 IU/kg): - - + + + - - + + +
p-AKT/t-AKT
ns
**
- insulin
+ insulin
VEH
KIRA8
C
Tunicamycin (ng/mL): 0 0 25 25 50 50 100 100 0
KIRA8 (1 μM): - - - + - + - + +
* 1 S
2 U
3 U
% XBP1s: 15 14 40 1 39 8 56 17 0
D
Palmitate (100 μM): - - + +
KIRA8 (1 μM): - - - +
* 1 S
2 U
3 U
% XBP1s: 3 2 17 5
E
Tunicamycin (ng/mL): 0 0 25 25 50 50 100 100 0
KIRA8 (1 μM): - - - + - + - + +
p-AKT Ser 473
total AKT
total IRE1α
BiP
GAPDH
Insulin (3 nM): - + + + + + + + +
F
Palmitate (100 μM): - - + +
KIRA8 (1 μM): - - - +
p-AKT Ser 473
total AKT
XBP1s
GAPDH
Insulin (100 pM): - + + +

FIGURE 1.2 KIRA8 restores AKT Ser473 phosphorylation in the insulin-sensitive tissue of BTBR*Lep*$^{ob/ob}$ mice and chemically/genetically induced ER stress *in vitro.*

A & B) Immunoblots for AKT Ser473 phosphorylation and total AKT in liver(A) or fat (B) tissues of 4 weeks KIRA8 and vehicle treated BTBR*Lep*$^{ob/ob}$ mice. For this specific experiment, mice were fasted for 18 hrs. and then stimulated with an IP injection of insulin (2 IU/kg). Each lane is from an individual mouse. Graphs represent signal intensity ratios. Bars represent means $\pm$ SEM. p values: * < 0.05, ** < 0.01.

C) ER stress was induced in HepG2 liver cells by a 24-hour treatment with tunicamycin at different concentrations in the presence or absence of KIRA8 (1 uM). Agarose gel of Pst1-digested XBP1 cDNA amplicons (radiometric quantitation of spliced to total XBP1 cDNAs. **D)** XBP1 splicing in H4IIEC3 cells subjected to palmitate in the absence or presence of KIRA8 for 24 hours in FBS-free media followed by insulin stimulation for 5 minutes. **E)** ER stress was induced in HepG2 liver cells by a 24-hour treatment with tunicamycin at different concentrations in the presence or absence of KIRA8 (1uM). Cells were subsequently stimulated with insulin (3 nM) for 10 minutes. AKT Ser473 phosphorylation and its total protein levels, total IRE1 α , and BiP were examined by direct immunoblotting. **F)** AKT Ser473 phosphorylation in H4IIEC3 cells subjected to Palmitate in the absence or presence of KIRA8 for 24 hours in FBS-free media followed by insulin stimulation for 5 minutes.

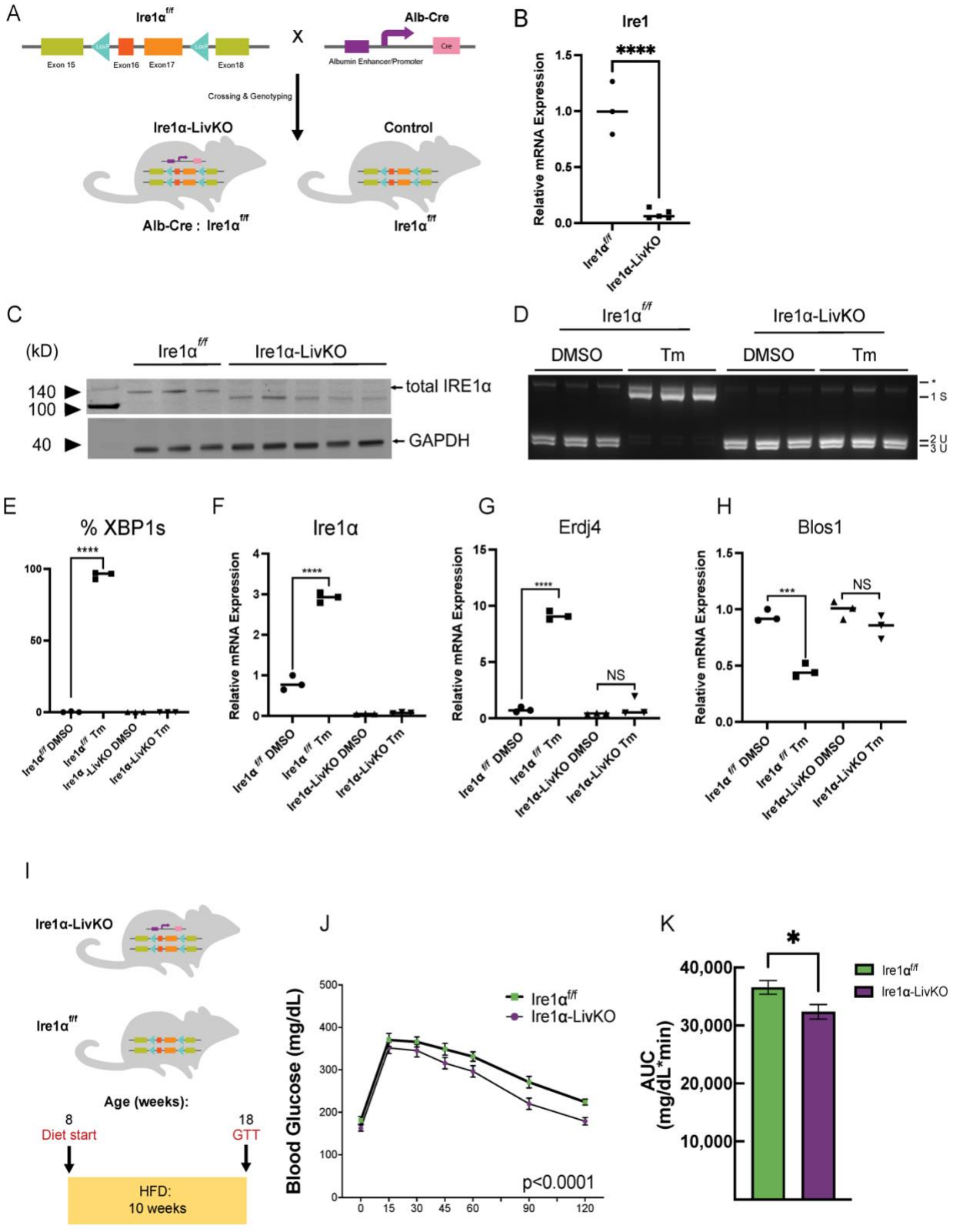
A
Ire1α f/f
Exon 15
Exon16
Exon17
Exon18
X
Alb-Cre
Albumin Enhancer/Promoter
Cre
Crossing & Genotyping
Ire1α-LivKO
Alb-Cre : Ire1α f/f
Control
Ire1α f/f
B
Ire1
****
Relative mRNA Expression
1.5
1.0
0.5
0.0
Ire1α f/f
Ire1α-LivKO
C
(kD)
Ire1α f/f
Ire1α-LivKO
140
100
40
total IRE1α
GAPDH
D
Ire1α f/f
Ire1α-LivKO
DMSO
Tm
DMSO
Tm
*
1 S
2 U
3 U
E
% XBP1s
****
100
50
0
Ire1α f/f DMSO
Ire1α f/f Tm
Ire1α -LivKO DMSO
Ire1α-LivKO Tm
F
Ire1α
****
Relative mRNA Expression
4
3
2
1
0
Ire1α f/f DMSO
Ire1α f/f Tm
Ire1α-LivKO DMSO
Ire1α-LivKO Tm
G
Erdj4
****
NS
Relative mRNA Expression
15
10
5
0
Ire1α f/f DMSO
Ire1α f/f Tm
Ire1α-LivKO DMSO
Ire1α-LivKO Tm
H
Blos1
***
NS
Relative mRNA Expression
1.5
1.0
0.5
0.0
Ire1α f/f DMSO
Ire1α f/f Tm
Ire1α-LivKO DMSO
Ire1α-LivKO Tm
I
Ire1α-LivKO
Ire1α f/f
Age (weeks):
8
Diet start
18
GTT
HFD:
10 weeks
J
Blood Glucose (mg/dL)
500
400
300
200
100
0
0
15
30
45
60
90
120
Ire1α f/f
Ire1α-LivKO
p<0.0001
K
*
AUC
(mg/dL*min)
40,000
30,000
20,000
10,000
Ire1α f/f
Ire1α-LivKO

FIGURE 1.3 Hepatocyte-specific IRE1α-deficient mice were successfully generated, and the reproducibility of the effect of KIRA8 on improving insulin resistance was confirmed.

A) Schematic of generation of Hepatocyte-specific IRE1α-deficient mice (IRE1α-LivKO). Floxed IRE1α (IRE1α$^{f/f}$**)** mouse was crossed with Alb-Cre mouse. **B)** The liver of IRE1α-LivKO and IRE1α$^{f/f}$ at 8 weeks of age and the expression levels of IRE1α were quantified by quantitative real-time PCR with GAPDH as control. **C)** Tissue lysates from IRE1α-LivKO and IRE1$^{f/f}$ liver were subjected to immunoblot analyses with antibodies against IRE1α and GAPDH. **D-H)** IRE1α-LivKO and IRE1$^{f/f}$ mice were fasted for 4 hours and Tunicamycin (Tm) was introduced with a dose of 0.5 mg/kg intraperitoneally. The liver was collected 5 hours after the administration of Tm. **D)** Agarose gel of Pst1-digested XBP1 cDNA amplicons **E)** Radiometric quantitation of spliced to total XBP1. **F-H)** Expression of IRE1α, Erdj4, and Blos1 were measured by quantitative real-time PCR with GAPDH as control. **I)** 8-weeks old IRE1α-LivKO or IRE1$^{f/f}$ were fed the HFD for 10 weeks. **J)** GTT assays were performed. Mice were fasted for 6 hours before glucose injection (2 g/kg). **K)** Area under the curve (AUC) for IPGTT.

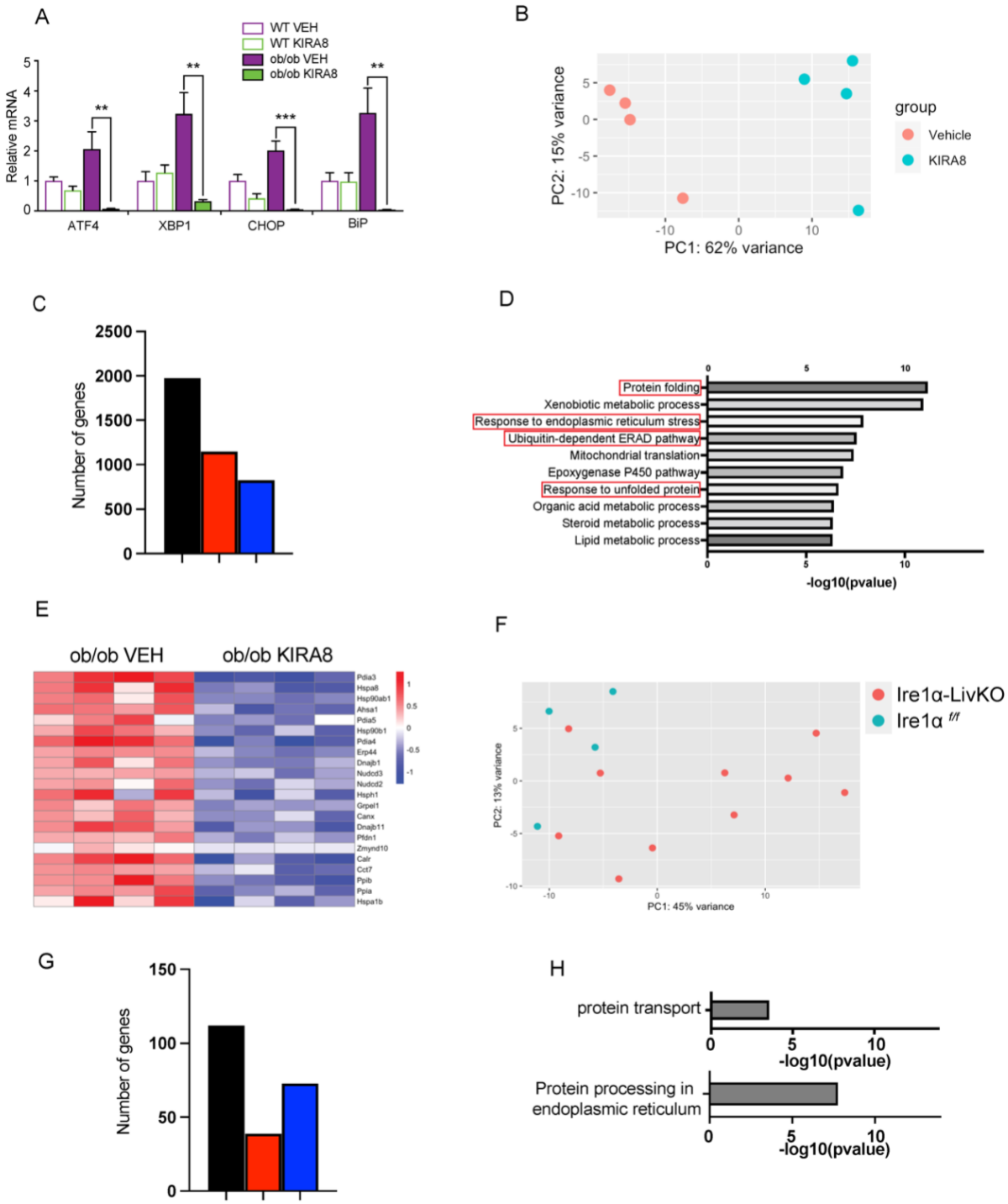
A
WT VEH
WT KIRA8
ob/ob VEH
ob/ob KIRA8
Relative mRNA
ATF4
XBP1
CHOP
BiP
B
PC2: 15% variance
PC1: 62% variance
group
Vehicle
KIRA8
C
Number of genes
D
Protein folding
Xenobiotic metabolic process
Response to endoplasmic reticulum stress
Ubiquitin-dependent ERAD pathway
Mitochondrial translation
Epoxygenase P450 pathway
Response to unfolded protein
Organic acid metabolic process
Steroid metabolic process
Lipid metabolic process
-log10(pvalue)
E
ob/ob VEH
ob/ob KIRA8
F
Ire1α-LivKO
Ire1α f/f
PC2: 13% variance
PC1: 45% variance
G
Number of genes
H
protein transport
Protein processing in endoplasmic reticulum
-log10(pvalue)

FIGURE 1.4 Reduction of mRNAs encoding proteins mediating ER protein folding by inactivation of IRE1α both by KIRA8 and genetic knockout.

A) Relative mRNAs levels in liver tissue from WT BTBR and BTBR*Lep*$^{ob/ob}$ mice treated with KIRA8 (50 mg/kg) or vehicle for 28 days. Bars represent means ± SEM. p values: * < 0.05, ** < 0.01, *** < 0.001. **B)** IPA Plot of RNA-Seq Data from KIRA8 or Vehicle Treated *obob* Mouse Liver. The Ingenuity Pathway Analysis (IPA) plot shows the significant pathways and biological processes affected by KIRA8 treatment compared to vehicle treatment in *obob* mouse liver samples. **C)** Number of Differentially Expressed Genes (DEGs) in KIRA8 treated mice liver compared to vehicle-treated BTBR*Lep*$^{ob/ob}$ Liver. Black: unchanged, Red: Increased; Blue: Decreased. **D)** Gene Ontology (GO) Analysis of downregulated genes (upper panel) and upregulated genes (lower panel) in KIRA8 Treated BTBR*Lep*$^{ob/ob}$ mouse liver compared to vehicle-treated ones. **E)** Heatmap of Gene Expression Levels in the Protein Folding Pathway. The heatmap shows the expression levels of genes involved in the protein folding pathway, selected from GO analysis of KIRA8-treated BTBR*Lep*$^{ob/ob}$ mouse liver samples compared to vehicle-treated samples. The rows represent individual genes, and the columns represent the treatment groups (vehicle or KIRA8). Red indicates higher expression levels, while blue represents lower expression levels. The color intensity corresponds to the degree of gene expression. The legend shows the color coding for gene expression levels. **F)** Ingenuity Pathway Analysis (IPA) Plot of RNA-seq Data in Hepatocyte-specific IRE1α-deficient Mice (IRE1α-LivKO) or Control mice (IRE1$^{f/f}$) Liver. **G)** Number of Differentially Expressed Genes (DEGs) in Hepatocyte-specific IRE1α-deficient Mice (IRE1α-LivKO) compared to Control mice (IRE1$^{f/f}$) Liver. Black: unchanged, Red: Increased; Blue: Decreased. **H)** Gene Ontology (GO) and Kyoto Encyclopedia of Genes and Genomes (KEGG) pathway analysis of downregulated genes in hepatocyte-specific IRE1α-deficient Mice (IRE1α-LivKO).

CHAPTER 2

Myeloid-Specific lRE1α Deletion Alleviates Non-Alcoholic Fatty Liver Disease-Associated Hepatic Fibrosis and Steatosis

ABSTRACT

Non-alcoholic fatty liver disease (NAFLD) is affecting as many as ~1-in-3 Americans. There are currently no medications approved to treat NAFLD. Moreover, complications such as hepatic insulin resistance manifest long before liver failure, and NAFLD is present in ~70% of type 2 diabetics. The mechanisms by which NAFLD develops are not well defined, but chronic nutrient excess is an implicated risk factor. Indeed, mice fed high fat and sugar diets recapitulates many NAFLD pathologies. In particular, so-called “Western” diets high in saturated fatty acids (SFA) induce ER stress in the liver, as well as activation and accumulation of hepatic macrophages. Notably, a gross depletion of myeloid cells reduces disease severity in mice. However, the role of macrophage-specific IRE1α in the pathogenesis of NAFLD remains largely unexplored. We hypothesize that, in the context of nutrient excess, myeloid-specific IRE1α mediates activation of inflammatory response within the liver in a manner essential for the progression of NAFLD. Moreover, we assessed the extent to which myeloid-specific IRE1α can be targeted to prevent established NAFLD-associated symptoms.

INTRODUCTION

The relentless global surge in obesity has given rise to a simultaneous increase in the prevalence of associated comorbidities. Among these comorbidities is NAFLD, a condition now impacting 25% of the global population and that is reaching alarming rates of approximately one in three Americans[62,63]. NAFLD has 4 stages of progression, comprising steatosis, steatohepatitis, fibrosis, and cirrhosis, which can ultimately lead to hepatocellular carcinoma[64]. Currently, there are no approved medications to address or prevent NAFLD, posing a substantial unmet need for this patient population[65].

Chronic diet-induced NAFLD in mice is characterized by hepatic ER stress and the activation and accumulation of myeloid cells, including both resident hepatic (Kupffer cells) and recruited (monocytes and macrophages) populations[66–68]. These myeloid cells play a pivotal role in driving NAFLD liver pathology, as demonstrated by the significant reduction in disease severity (e.g. hepatic steatosis and insulin resistance) upon gross depletion of myeloid cells[69]. Our lab showed that SFAs, a dietary nutrient that is commonly associated with fatty livers, activate IRE1α and subsequently the NLRP3-IL-1β pathway[70]. This pathway that is highly implicated in the pathogenesis of NAFLD[71–76]. A recent study demonstrated that mice with NLRP3 deletion in myeloid cells were protected from fibrotic nonalcoholic steatohepatitis[76]. These data prompt us to assess the impact of IRE1α as an upstream activator of the NLRP3 pathway in the context of diet-induced NAFLD progression

Understanding the liver's functional architecture is crucial for comprehending NAFLD pathogenesis. Two key features in hepatic micro-architecture are the portal triad and the central vein. The portal triad comprises the hepatic artery, portal vein, and bile duct, while the central vein returns deoxygenated blood to the systemic circulation. The space between these structures establishes gradients critical to the liver's diverse physiological functions. Hepatocytes can be categorized into three zones based on

these landmarks. Zone 1 hepatocytes, closest to the portal triad, experience high oxygen levels and are the first to encounter absorbed nutrients, toxins, and pathogens. Zone 3 hepatocytes engage in processes like glycolysis, lipogenesis, and xenobiotic metabolism[77]. Zone 3 hepatocytes are often the initiation sites for steatosis in adult fatty livers, manifested as the ballooned hepatocytes[78]. Zone 2 hepatocytes, though less defined metabolically, contribute significantly to liver homeostasis[77].

In this chapter, we evaluate the impact of myeloid IRE1α on NAFLD-associated steatosis and fibrosis. Additionally, we investigate whether the deletion of IRE1α in myeloid cells influences systemic glucose homeostasis.

RESULTS

Genetically Deleting IRE1α in Myeloid Compartment Does Not Affect Hepatic Immune Cell Composition and Normal Development

To establish the myeloid-specific IRE1α deletion mouse model (IRE1α -MacKO), we crossed previously introduced IRE1α $^{f/f}$ mice with those expressing Cre recombinase under the control of a myeloid-specific *Lyz2* promoter (*LysM*-Cre) (**Figure 2.1A**). IRE1α $^{f/f}$ littermates (WT), lacking the Cre allele, served as the control group. The KO efficiency was confirmed by RT-qPCR of FACS-sorted CD64+ liver macrophages (**Figure 2.1B**), with significantly reduced *Ern1* and *Xbp1* expression compared to that of WT control samples (**Figure 2.1B**). Moreover, we assessed the functionality of IRE1α KO in *ex vivo* differentiated macrophages by stimulating bone marrow-derived macrophages (BMDMs) with tunicamycin. IRE1α-MacKO BMDMs displayed suppressed XBP1 splicing activity, further validating the functional KO model (**Figure 2.1C**). Importantly, there was no observable difference between IRE1α-MacKO BMDMs and WT BMDMs in their ability to differentiate.

Given the critical role of macrophages in the immune system and their potential impact on liver immune cell composition, we investigated the consequences of IRE1α deletion under metabolic challenge. Flow cytometry on stromal vascular fraction (SVF) isolated from livers of IRE1α-MacKO and WT mice on a 16-week Gubra-Amylin NASH (GAN) diet revealed no significant differences in macrophage numbers or immune cell composition (**Figure 2.1D**). Subsequently, we assessed the total body and metabolic tissue weights of IRE1α-MacKO and WT mice subjected to either 8 or 16 weeks of GAN diet. While the GAN diet led to a substantial increase in total body, adipose tissue, and liver weights (**Figure 2.1E-G**), IRE1α-MacKO mice maintained comparable weight measurements to WT groups under the same dietary regimen. Notably, IRE1α-MacKO liver weights from the 16-week GAN group were significantly lower than those of the WT group, without noticeable differences in liver sizes (**Figure 2.1G**).

In summary, our study successfully validated the KO efficiency in the IRE1α-MacKO model. Furthermore, we demonstrated that IRE1α deletion does not alter liver immune cell composition or whole-body development. Intriguingly, IRE1α deletion appears to mitigate further liver weight gain under chronic dietary challenge.

Myeloid-specific IRE1α Deletion Does Not Impact Systemic Glucose Homeostasis
From the Chapter 1 study, we learned that IRE1α systemic inhibition using KIRA8 and hepatocyte-specific IRE1α KO prevents hyperglycemia. However, the role of myeloid cell IRE1α in regulating glucose homeostasis remained unexplored. Therefore, we performed GTT on IRE1α-MacKO and WT mice that were on GAN diet for 16 weeks. The myeloid-specific deletion of IRE1α was found to have no impact on systemic glucose homeostasis (**Figure 2.2A**). Despite the induction of glucose intolerance in response to a GAN diet, IRE1α-MacKO mice did not show differentiation from the WT group, and the calculated AUC was not significantly different between the two genotypes (**Figure 2.2B**). In summary, the specific deletion of IRE1α in myeloid cells did not affect systemic glucose homeostasis under the conditions tested.

Myeloid-specific IRE1α Deletion Does Not Alter Overall Abundance of Hepatic Steatosis but Induces a Shift In The Zonal Distribution
To examine one facet of NAFLD that is hepatic steatosis, we performed Oil red O (ORO), a marker for neutral lipids, staining on liver tissue sections from 8-week old mice on GAN diet (**Figure 2.3B**). The analysis revealed that the total ORO-positive area and average lipid droplet size across the entire liver sections were comparable between IRE1α-MacKO and WT animals, suggesting that the gross lipid deposition in the livers remained unaffected following IRE1α deletion (**Figure 2.3 A&B**). However, upon specific evaluation of the periportal region (defined as the area within 4 hepatocytes from the portal veins), we observed a significant reduction in the ORO-positive area in IRE1α-MacKO compared to WT (**Figure 2.3C**). Notably, while both genotypes exhibited large LDs in hepatocytes near central veins, the lipid droplets were noticeably smaller in the periportal regions of IRE1α-MacKO compared to those of WT mice(**Figure 2.3D**). In summary, our data suggest that the deletion of IRE1α in myeloid cells results in an amelioration of steatosis specifically in zone 1 – the periportal area.

Myeloid-specific IRE1α Deletion Mitigates NAFLD-Associated Fibrosis
The progression of NAFLD is often linked to an escalation in hepatic fibrosis due to the accumulation of collagen deposition mostly by hepatic stellate cells (HSCs)[64]. To investigate the impact of myeloid-specific IRE1α deletion on this process, we assessed liver fibrosis performed with picrosirius red staining on liver sections from in mice subjected to 8 or 16 weeks of the GAN diet (**Figure 2.4A**). Our observations revealed a substantial induction of collagen fibers in response to the GAN diet, with a notable reduction in collagen deposition observed in mice with myeloid-specific IRE1α deletion (**Figure 2.4A**). Quantification of the picrosirius red-positive area further confirmed that the diet-induced collagen deposition was significantly mitigated in the IRE1α-MacKO mice (**Figure 2.4B&C**). Additionally, the hydroxyproline assay, a method for quantifying fibrillar collagen, provided conclusive evidence of a significant reduction in collagen content in IRE1α-MacKO livers compared to WT in the 8-week-GAN group (**Figure 2.4D**). In summary, our data strongly suggest that the deletion of IRE1α within the myeloid compartment imparts notable benefits in countering hepatic fibrosis associated with NAFLD.

DISCUSSION

In this study, we have demonstrated the critical role of myeloid IRE1α in the pathogenesis of NAFLD. Our previous findings demonstrated that genetic IRE1α deletion in hepatocytes protects mice from hyperglycemia. Surprisingly, we did not observe any significant differences in glucose tolerance or fasting glucose levels between the genotypes. Interestingly, a study by Canpenhout et al. reported contradictory results: in their myeloid-specific IRE1α deletion mouse models of diabetes induced by streptozotocin followed by 17 weeks of a western diet, the KO mice displayed lower fasting glucose levels and improved glucose tolerance[79]. The inconsistency between our data and theirs could potentially be attributed to differences in diets and models. Strikingly, their mouse model displayed more severe hyperglycemia, suggesting a potential glycemic protection mechanism that is uniquely beneficial for severely diabetic mice.

Our study showed that deletion of IRE1α in myeloid cells effectively prevents NAFLD-associated steatosis and fibrosis. We observed a reduction in lipid droplet deposition and size specifically in the periportal regions, referred to as Zone 1 of hepatic lobules. This finding is significant, especially considering that, in obesity-induced NAFLD livers, steatosis primarily occurs in the pericentral regions (Zone 3), progressing towards Zone 1 as the disease advances[78,80]. Our observation led us to hypothesize that the deletion of IRE1α in myeloid cells alters the macrophage-to-hepatocytes crosstalk, resulting in reduced ER stress and decreased activation of pro-inflammatory pathways. Intriguingly, several studies have implicated the involvement of the NLRP3-IL-1β pro-inflammatory axis in hepatic steatosis, providing additional support for the idea that deleting IRE1α in macrophages contributes to the reduction of hepatic inflammation and steatosis[74,81,82]. To test this hypothesis, we can isolate macrophages from IRE1α-MacKO and WT mice. These macrophages can then be co-cultured with primary hepatocytes in a NASH-mimic media supplemented with glucose, insulin and free fatty acids. This co-culture setup aims to confirm the lipid-loading phenotype and allows for the profiling of hepatocyte transcriptional changes. Moreover, we plan to implement a cell type-specific proximity biotinylation strategy, utilizing the engineered ER-TurboID construct[83], to uncover novel secreted proteins originating from myeloid cells. This will shed light on the mechanism driving the hepatocyte patho-etiology in endocrine and paracrine manner.

Furthermore, our study revealed that myeloid-specific IRE1α deletion effectively alleviated NAFLD-associated fibrosis in the context of an 8-week-GAN regimen. In obesity-induced NAFLD livers, fibrosis typically initiates in the Zone 3 perisinusoidal area (NAFLD Stage 1) and progresses to involve both Zone 3 and Zone 1 as the disease advances (NAFLD Stage 2)[64]. The lack of difference between genotypes in the 16-week-GAN hydroxyproline assay could be attributed to a plateauing effect at the later stages of NAFLD, where extensive bridging fibrosis connecting central and portal veins may occur. This phenomenon potentially saturated the collagen deposition in the tissues, making it challenging to detect differences in collagen content between genotypes at this later stage. To gain further insights into the stage of NAFLD,

assessing the morphological and zonal distribution of fibrosis would be beneficial. This approach will help elucidate our understanding of how IRE1α deletion influences the pathogenesis of NAFLD, particularly in terms of fibrosis progression and distribution. Lastly, employing a co-culture model with KO and WT macrophages along with primary hepatic stellate cells (HSCs) could further provide valuable insights into the mechanisms underlying the anti-fibrotic phenotype associated with IRE1α deletion in macrophages.

A significant limitation of our IRE1α-MacKO model is that IRE1α KO occurs in all LysM-expressing tissues. This includes myeloid cells in other metabolic tissues, such as adipose tissues, which could potentially influence hepatic NAFLD-associated phenotypes in an endocrine manner. To address this issue and specifically assess the effect of IRE1α perturbation in hepatic resident macrophages, we have introduced the Kupffer cell-specific Cre mouse line (Clec4f-Cre-tdTomato) into the IRE1α f/f background. In the advanced stages of NAFLD, Kupffer cells undergo high turnover, during which newly recruited macrophages replace the existing macrophage populations. Therefore, we also aim to examine the extent to which IRE1α deletion in infiltrated macrophages contributes to preventing NAFLD using the Ms4a3-Cre line (courtesy of Dr. Ginhoux, Singapore Immunology Network)[84] . This optimized approach will allow us to better understand the sub-populations of hepatic resident macrophages in the context of IRE1α-mediated effects on NAFLD.

In summary, our study shows that myeloid-specific IRE1α deletion provides protection against NAFLD-associated steatosis and fibrosis. This suggests that IRE1α could be a potential therapeutic target for NAFLD, particularly through approaches like nanoparticle delivery that facilitates targeted treatment to the liver[85].

MATERIALS AND METHODS

Mouse Studies

IRE1α conditional KO mice (IRE1α$^{f/f}$) was acquired from the Kaufman lab, Sanford Burnham Prebys, San Diego, CA. Mice were genotyped using the primer sequences: 5′-CAGAGATGCTGAGTGAAGAC-3′, and 5′-ACAGTGGTTCCTGTGAAGGT-3′. The floxed allele generates 241-bp band and WT allele generates 377-bp band. LysM-Cre mice [B6.129P2-*Lyz2*$^{tm1(cre)Ifo}$/J, myeloid specific recombination] were obtained from Jackson Laboratories (stock numbers: 004781). LysM-Cre mice were genotyped by following the instruction of Jackson Laboratories. To generate diet induced obesity, IRE1α-MacKO and WT mice were fed a GAN high fat diet with 40 kcal% Fat (Palm Oil), 20 kcal% Fructose and 2% Cholesterol (Cat #: D09100310; Research Diet INC.), for either 8 weeks or 16 weeks starting at 8 weeks of age. All procedures were performed in accordance with protocols approved by the Institutional Animal Care and Use Committee at the University of California, San Francisco. Animals were kept in a specific pathogen-free animal facility on a 12 hr light- dark cycle at an ambient temperature of 21°C. They were given free access to water and food.

Glucose Tolerance Tests

IRE1α-MacKO and WT control mice were fasted for 6 hours before IP injection with glucose (2g/kg). Blood was collected from the tail vein after an initial small tail clip, and glucose levels were determined using LifeScan glucose meter (OneTouch Ultra). Concentrations of reagents are specified in figure legends.

Histology

Oil Red O (ORO) staining: Liver lobes were collected post-perfusion and fixed overnight in 4% paraformaldehyde (PFA) at 4°C with rocking. Subsequently, they were transitioned to 30% sucrose for dehydration and storage at 4°C. Dehydrated liver samples were then sectioned into smaller pieces and embedded in OCT (Tissue-Tek®). Tissues OCT blocks were stored at -20°C for short-term use or at -80°C for long-term storage. The OCT-embedded liver samples were cryo-sectioned at a thickness of 10 um and mounted on slides for further analysis. The stock ORO solution is prepared by saturating 0.3g of ORO powder (Sigma Al, Cat #:O0625) in 10 ml of 100% isopropanol in a beaker. The beaker is sealed and let stand in dark for 3 days at room temperature. Agitate the mixture and centrifuge for 15 minutes at 900 x g at RT. Transfer the liquid supernatant into a new tube and store the stock ORO up to 6 months at RT. For ORO working solution dilute stock with distilled water at 6:4 ratio (ORO stock to water). Mix the solution well and filter through 0.45 um filter. The working ORO solution can be stored up to 6 months at RT. The slides with frozen sections were completely dried at RT for at least 30 min before fixing again with 10% neutral buffered formalin for 10 minutes. Rinse off fixative with distilled water for 5 min at RT. Place sections in 100% propylene glycol for 2 min to dehydrate at RT. Stain in ORO working solution for 1 hour at RT (or 30 min at 37°C or 20 min at 60°C). Moves the slides to 85% propylene glycol (in distilled water) for 1 min at RT. Rinse with distilled water 2 times for 1 min each. Stain with Mayer's hematoxylin (Sigma Aldrich, Cat. # MHS32) for 2 minutes at RT. Wash with warm tap water for 2 min. Rinse with distilled water 2 times to get rid of excess hematoxylin stain. Air dry the slides at RT. Apply the coverslips with VectaMount® AQ Aqueous Mounting Medium (H-5501-60).

Picrosirius staining: Liver lobes were collected and fixed in 10% neutral buffered formalin overnight at RT followed by 70% ethanol dehydration the next day. Liver samples were paraffin-embedded following standard paraffin embedding protocol and sectioned at 10um thickness. Prepare Picrosirius Red solution by dissolving 0.5 g Sirius red F3B (AKA "Direct Red 80", Catalog # 36-554-8) in 500ml of saturated aqueous solution of picric acid. Paraffin-embedded tissue slides were incubated at 60°C for 1 hour to melt paraffin. Deparaffinize in Xylene and ethanol following standard protocol (Xylene → 100% EtOH→ 95% EtOH → 70% EtOH). Wash with PBS for 3 minutes. Stain nuclei with Weigert's Hematoxylin (Sigma Aldrich, Cat. # HT1079) for 11 minutes. Rinse the slides in running tap water for 1-2 minutes. Stain slides with Picrosirius Red for 1 hour. Wash slides in 2 changes of acidic tap water (5 mL glacial acetic acid to 1 L of tap water) for 5 minutes. Remove most of the glacial acetic water off slides by shaking. Dehydrate the slides in ethanol and xylene (70% EtOH→95% EtOH→100% EtOH→ Xylene). Mount slides using CytoSeal mounting median and cover with coverslip.

Microscopy & ImageJ quantification
Images for both ORO and picrosirius red staining were acquired using Keyence All-in-One Microscope (BZ-X810) with 20x lens. Brightfield ORO images were stitched 5x5 and converted to RGB stack in ImageJ. Proper threshold was applied uniformly across all samples. Using particle analysis function to quantify ORO-positive signals. For periportal ORO quantification, signals within 4 hepatocytes away from portal veins were quantified. For picrosirius red staining, images were acquired through brightfield and Texas Red (560/40) filters were stitched 7x7. The images acquired at fluorescent channel were quantified using ImageJ similar to ORO staining quantification.

Hydroxyproline Assay for Collagen Content
~100mg of liver tissue was used and the weights were recorded. Hydroxyproline assay was perform following manufacturer protocol (QuickZyme Hydroxyproline Assay Kit, Cat. #: QZBHYPRO). The collagen content was normalized to the tissue weights (ug/mg).

RNA Isolation, Quantitative Real-Time PCR, and Primers
RNA was isolated from tissue using TRIzol (Invitrogen) followed by RNeasy kit (Qiagen, Cat.# 74004) protocol. Up to 1 µg total RNA was reverse transcribed into cDNA using the SensiFast™cDNA synthesis kit (Meridian Bioscience, Cat.# BIO-65054). Differences in relative gene expression were quantified by qRT-PCR using SYBR Green (QIAGEN) and StepOnePlus Real-Time PCR System (Applied Biosystems). Thermal cycles were: 5 min at 95°C, 40 cycles of 15 s at 95°C, 30 s at 60°C. Gene expression levels were normalized to hypoxanthine guanine phosphoribosyltransferase (HPRT) housekeeping gene. Sequences of primers used for qPCR can be found in **Table 2.1**.

Liver Leukocyte Isolation & FACS
After perfusion, a piece of liver per mouse was weighed and minced in 1 ml of cold RPMI. Samples were transferred 50ml conical tubes with additional 2 ml of RPMI. 1ml of digestion buffer (Collagenase IV 2.5mg/mL, Collagenase II 3.4mg/mL protease 4mg/mL, and DNase 4mg/mL all dissolved in RPMI) was added to each tube, followed by incubation for 30 minutes in shaker at 37°C. Then, the livers were mashed through 100 um strainers into new 50 mL conical tube with 10 mL syringe plunger. Flush with FACS buffer (2% FBS and 2mM EDTA in PBS without Ca/Mg) until most of cells pass through the filter. Fill up to 45ml with FACS buffer and centrifuge at 500 x g for 5 minutes at 4°C. The supernatant was discarded. Pellets were resuspended with 45 mL of FACS buffer and centrifuge at 500 x g for 5 minutes at 4°C. The supernatant was discarded, and the pellet was in 20mL of 33% Percoll (5.94ml of Percoll + 66ul of 10x PBS + 11.4mL of RPMI) and centrifuged at 850 x g with minimum break & accelerator for 15 minutes at 4°C. Carefully remove the top layer hepatocytes and dilute remaining15-20 mL of supernatant & pellet with FACS buffer up to 45 mL. Centrifuge 5 min at 800 x g at 4ºC and discard supernatant. The pellet was respended in 2mL ACK lysis buffer at RT by vortexing and incubate for 3 min on ice. The Lysis reaction was quenched with 18mL FACS buffer and centrifuged at 500 x g for 5 minutes at 4°C. The supernatant was discarded. Cell pellets were resuspended in 400 uL FACS Buffer (with FC Block at 1:200), and transfer to filter-cap FACS tube passing through 35um mesh

cap. Perform cell count and adjust the cell number to be around 1 million per tube. Stain cell with antibody mixture (**Table 2.2**) in dark for 30 minutes at 4°C. Wash by diluting with 3 mL of FACS buffer and centrifuge at 500 x g for 5 minutes at 4°C. The cell pellets were resuspended in 300-400uL of FACS buffer with DAPI at final concentration 0.25ug/mL as viability stain. Add 50uL of counting beads per samples (typically around ~50,000 beads) to each sample. FACS machine used is BD FACSAria II Cell Sorter (UCSF Flow Cytometry Core).

Statistical Analysis

All statistical analyses were performed using GraphPad Prism version 8.1 software. Student's t test or two-way ANOVA were applied to determine statistical difference between two groups. Data are presented as mean ± SEM. Significance was defined by a p value < 0.05. p values: * < 0.05; ** < 0.01; *** < 0.001; NS, non-significant.

TABLE 2. 1 List of primers in RT-qPCR in FACS-sorted mouse liver macrophages.

Gene	Forward Primer	Reverse Primer
Ern1	CCCATCACCCTGCTTCATCA	TGCAGAGGCCAAAGTCAGAG
sXbp1	GACAGAGAGTCAAACTAACGTGG	GTCCAGCAGGCAAGAAGGT
HPRT	TCAGTCAACGGGGGACATAAA	GGGGCTGTACTGCTTAACCAG

TABLE 2. 2 List of antibodies in flow cytometry and FACS.

Antibody	Source (Catalog number)	Dilution
Ly6C-AF488	BioLegend, 128022	1:200
CD45-Percp Cy5.5	BioLegend, 103132	1:400
CD19-PE Dazzle 594	BioLegend, 115553	1:80
CD3-PE Cy7	BioLegend, 100219	1:400
CD64-AF647	BioLegend, 139322	1:400
Ly6G-APC Cy7	BioLegend, 127623	1:400

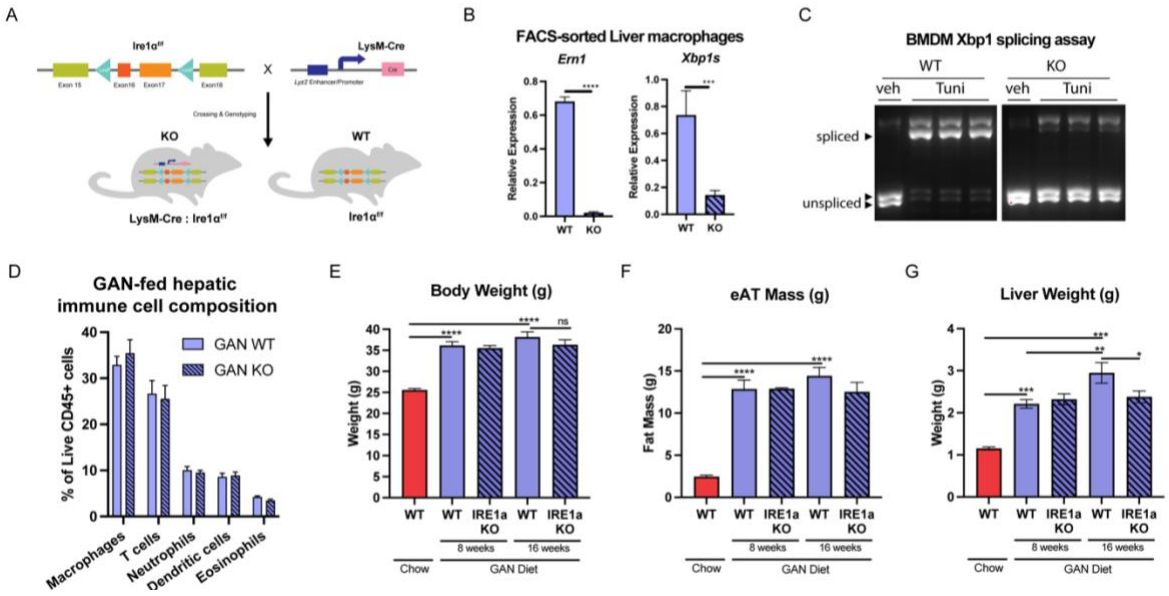

FIGURE 2.1 Genetically deleting IRE1α in myeloid compartment does not affect hepatic immune cell composition and normal development.

A) Schematic of generation of myeloid-specific IRE1α-deficient mice (IRE1α-MacKO). Floxed IRE1α (IRE1α$^{f/f}$) mouse was crossed with LysM-Cre mouse. **B)** Gene expression analysis on *Ern1* and spliced *Xbp1* of FACS-sorted macrophage from livers isolated from mice fed on GAN diet for weeks (n=4-7). Two-tail T test was performed. **C)** Xbp1 splicing assay of BMDMs isolated from IRE1α-MacKO and WT mice that were 8-10 weeks of age. Cells were treated with Tunicamycin at 5ug/mL (Tuni) or DMSO (Veh.) for 16 hours. **D)** FLOW-based immune cell profiling of liver stromal vascular fractions isolated from mice fed on GAN diet for 24 weeks starting at 8 weeks of age (n=7). **E-G)** Body weights (E), epididymal adipose tissue (eAT) mass (F) and liver weight (G) of Chow WT (n=13) 8-week-GAN (n=8) 16-week-GAN (n=11-13) mice. Ordinary one-way ANOVA test was performed. (*:P<0.05, **: P<0.01, ***: P<0.001, ****: P<0.0001).

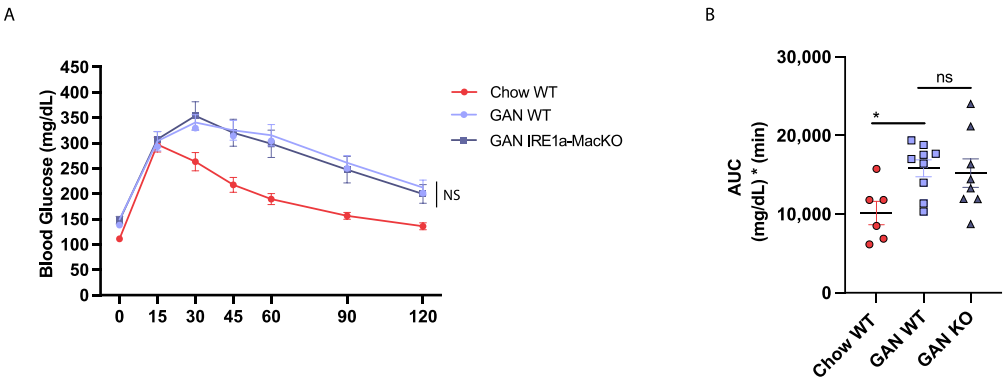

FIGURE 2.2 Myeloid-specific IRE1α deletion does not impact systemic glucose homeostasis.

A) GTT assays were performed. Mice were fasted for 6 hours before glucose injection (2 g/kg). **B)** Area under the curve (AUC) for IPGTT. Two-tail T test was performed.

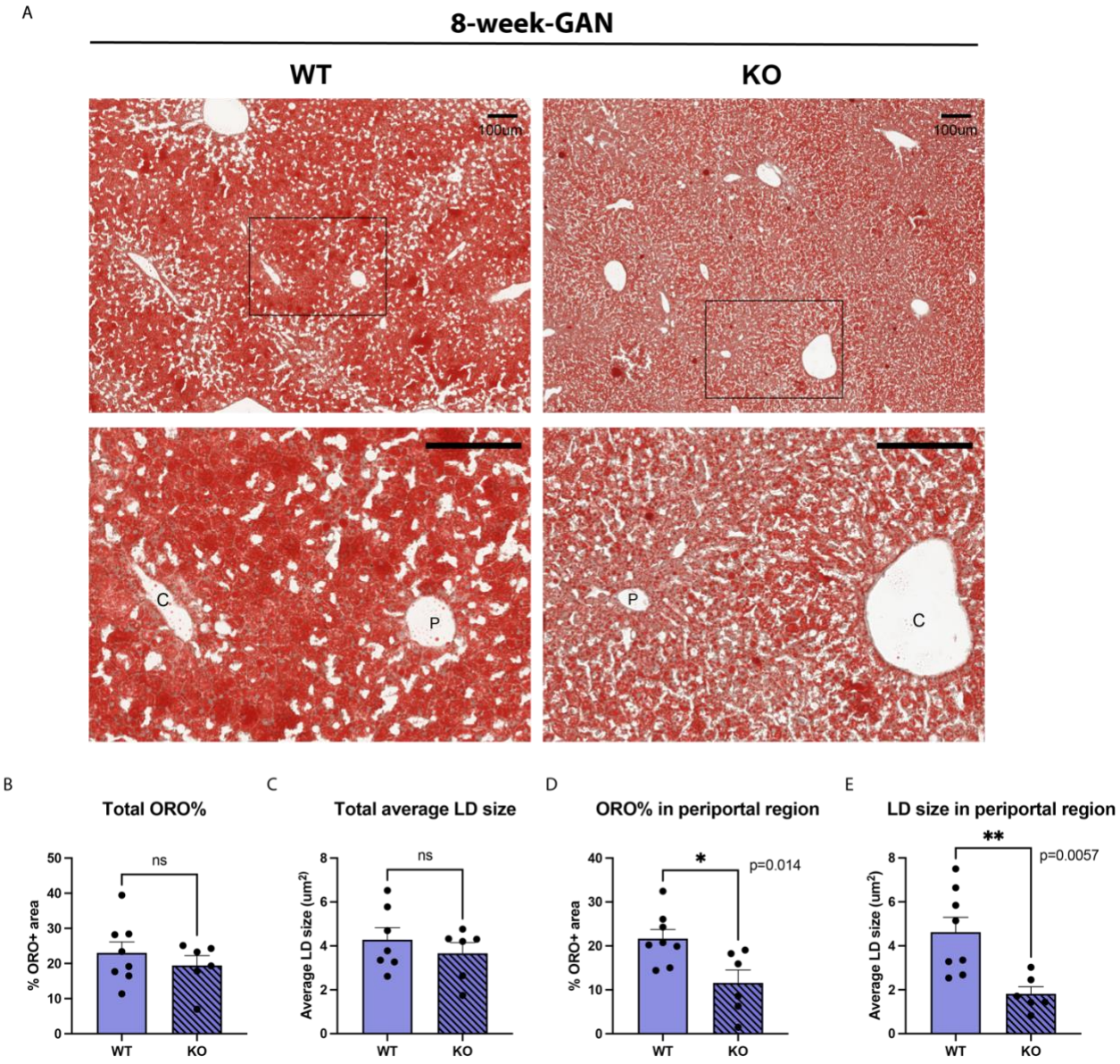

FIGURE 2.3 Myeloid-specific IRE1α does not alter overall abundance of hepatic steatosis but induces a shift in the zonal distribution.

A) ORO staining on liver sections from WT and IRE1α-MacKO mice fed on GAN diet for 8 weeks starting at 8-week-old. Scale bar represents 100um. P: portal vein. C: central vein. **B)** Percentage of total ORO area of the total section area. **C)** Average size of lipid droplets of the total section. **D)** Percentage of ORO area in the periportal regions. **E)** Average of lipid droplet size on the periportal regions. n=6-8. Two-tail T test was performed (*:P<0.05, **: P<0.01).

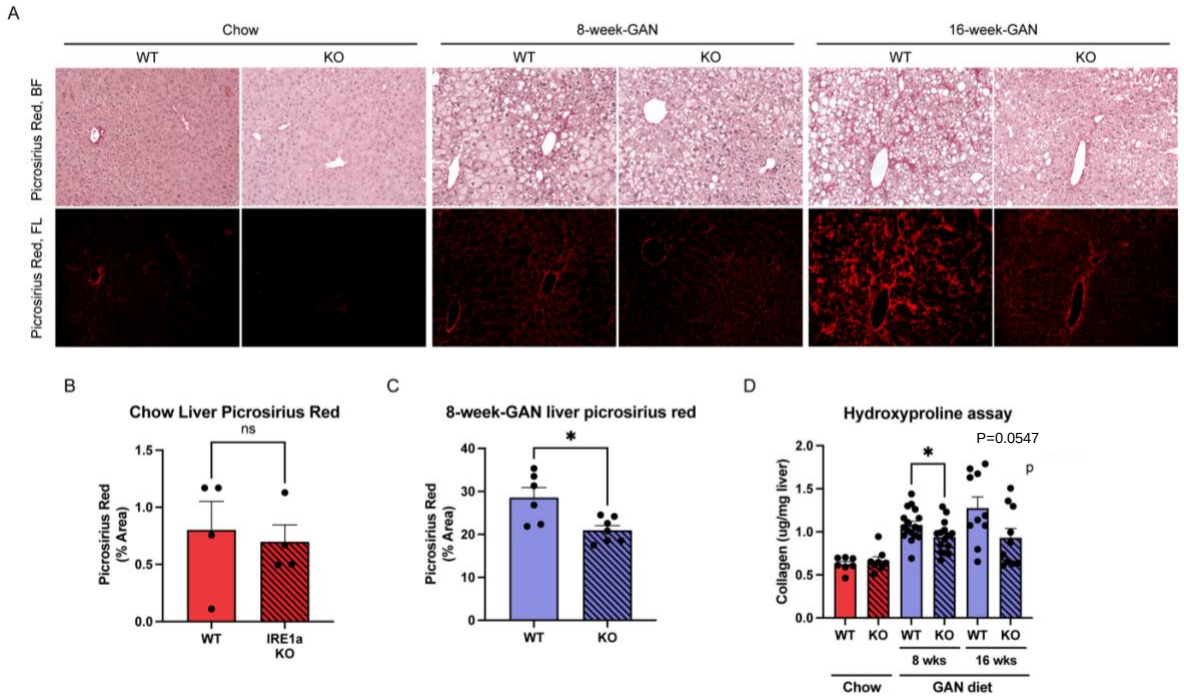

FIGURE 2.4 Myeloid-specific IRE1α deletion mitigates NAFLD-associated fibrosis.

A) Picro Sirius red staining of liver sections from chow, 8-week-GAN and 16-week-GAN diet-fed WT and IRE1α-MacKO mice. Top panels: bright field; bottom panels: Texas Red (560/40). **B-C)** Fibrosis quantification on picro sirius red staining of chow-fed (B) and 8-week-GAN (C) liver sections. Chow: n=4; 8-week-GAN: n=6-7. **D)** Hydroxyproline assay of liver tissues from chow (n=7-8), 8-week-GAN (n=15-17) and 16-week-GAN (n=10) diet-fed WT and IRE1α-MacKO mice.

CHAPTER 3

Myeloid-Specific IRE1α Deletion Prevents Atherosclerosis-Associated Plaque Expansion and Vascular Smooth Muscle Cell Proliferation

ABSTRACT

Atherosclerosis is a major driver of cardiovascular disease and a leading cause of death worldwide. It is an inflammatory disease caused in part by chronic saturated fat consumption. Vascular macrophages undergo inflammatory activation in response to the uptake of specific lipids, including saturated fats. The past few decades have revealed that macrophages in atherosclerotic plaques experience ER stress and induce the UPR. However, the role that IRE1α, specifically in macrophages, plays in the advancement of atherosclerotic lesions remains unexplored. We hypothesize that IRE1a activation specifically in macrophages is critical for atherosclerosis progression. Leveraging two dedicated myeloid-specific IRE1α deletion mouse models of atherosclerosis, we showed that deficiency of IRE1α in myeloid compartment protects mice from atherosclerotic lesion expansion and vascular cell proliferation.

INTRODUCTION

Atherosclerosis is an inflammatory disease caused by chronic saturated fat consumption and elevated plasma LDL-cholesterol[86]. While current treatment modalities and ongoing research focus on lowering circulating LDL-cholesterol (LDL-c) and raising HDL-cholesterol (HDL-c)[87–89], anti-inflammatory strategies to mitigate atherosclerosis are also emerging.[90] Specifically, the CANTOS trial showed that canakinumab, an anti-interlukin-1β (IL-1β) antibody, conferred cardiovascular protection without lowering LDL-c[90,91]. This raises an important question: can the cells and pathways responsible for producing IL-1b in atherosclerosis be manipulated to attenuate vascular inflammation?

Macrophages and vascular smooth muscle cells (VSMCs) are the two most abundant cell types in atherosclerotic plaques. Vascular macrophages undergo inflammatory activation in response to specific lipid uptake and become lipid-laden “foam cells”. Meanwhile, VSMCs, in response to increasing inflammatory signals, undergo proliferation and collagen deposition, leading to enlargement and stiffness of plaques[92]. Macrophages mediate atherosclerotic vascular inflammation by secreting several pro-inflammatory cytokines[21,93]. The gathering of lipid-laden "foam cells" in the vascular intima results in the formation and instability of plaques, elevating the risk of acute events[94].

Previous work has shown that lipid-laden “foam cells” within atherosclerotic plaques shift from being cytoprotective, phagocytic “scavengers” to pro-inflammatory and even necrotic cell types[95,96]. Moreover, blocking IRE1α kinase downstream signaling prevents atherosclerosis progression[97]. While Tufanli et al. demonstrated that systemic delivery of a IRE1α inhibitor drug could prevent atherosclerotic plaque expansion in mice[98], we aim to elucidate the cell-specific mechanisms responsible for these anti-atherogenic effects.

In this chapter, we assess the role of macrophage IRE1α in regulating atherosclerosis progression in the myeloid-specific IRE1α deletion mouse model with atherogenic genetic and dietary manipulation.

RESULTS

IRE1α Myeloid Deletion Attenuates Overall Atherosclerotic Lesion Expansion in AAV8-PCSK9-Induced Mouse Model of Atherosclerosis

To induce hypercholesterolemia, we administered tail-vein injections of AAV8-PCSK9 (D377Y, a gain-of-function mutation) to both IRE1α-MacKO and WT mice. One week post-injection, the mice were placed on a western diet (WD) for a total of 13 weeks to induce atherosclerotic plaque development (**Figure 3.1A**). Throughout the dietary regimen, no significant difference in weight gain was observed between the two genotypes (**Figure 3.1B**). To evaluate the severity of atherosclerosis, en face-prepared aortae were subjected to ORO staining to visualize atherosclerotic lesions (**Figure 3.1C**). While no notable differences between the genotypes were observed in lesion area in the ascending aorta, aortic arch, and descending aorta, the IRE1α-MacKO group exhibited visibly fewer lesions in the abdominal aorta. Quantification of ORO+ area confirmed significantly reduced lesion area in IRE1α-MacKO mice compared to WT (**Figure 3.1C**).

Recognizing obesity as a driving factor in atherosclerosis, despite no discrepancy in body weight, both genotypes displayed wide variations in weight gain, potentially influenced by cage-specific effects on group-housed mice (ranging from 34-44g). To elucidate the relationship between atherosclerotic lesion development and obesity, a correlation test was conducted. Interestingly, the data revealed a positive correlation between lesion area in KO mice and body weight (R^2=0.9527), whereas lesion area in WT mice displayed no correlation with body weight, indicating high lesion area at any body weight (**Figure 3.1D**). This suggests that IRE1α myeloid deletion impeded lesion expansion in a relatively lean state, whereas WT mice had already developed extensive lesions, and the protective phenotype was eventually masked with the progression of obesity.

The aortic root is particularly susceptible to atherogenic developments, primarily attributed to the elevated blood flow turbulence in this region, leading to increased aortic wall shear stress. Therefore, we also assessed the plaque area by performing ORO staining on aortic root sections (**Figure 3.1E**). Interestingly, we found that the plaque lesion (ORO+) area did not differ between genotypes (**Figure 3.1F**). Macrophages and VSMCs are the major cell types comprising plaques[99]. To further understand the composition of plaques, we conducted immunofluorescence staining on aortic root cross sections. Similarly, we found no difference in CD68+ macrophage area and αSMA+ VSMC area, suggesting that the plaque cell type compositions were not different between the two genotypes.

Taken together, AAV8-PCSK9 IRE1α-MacKO mice exhibited an overall reduction in lesion area in the aortae compared to the WT group and the protective effect was more pronounced in leaner animals. However, when specifically examining the aortic root region, neither plaque lesion area nor plaque compositions showed significant

differences, suggesting that these regions may have reached a saturation point for atherosclerotic plaques.

IRE1α Myeloid Deletion Ameliorates Atherosclerosis and Reduces Vascular Proliferation in Triple Transgenic Model of Atherosclerosis

In parallel with the AAV8-dependent model, we established a triple transgenic myeloid-specific IRE1α deletion model of atherosclerosis by crossbreeding IRE1α-MacKO with $Ldlr^{-/-}$ (LDL receptor null) mice. $IRE1\alpha^{f/f}$, $Ldlr^{-/-}$ mice served as the WT control, and the mice were placed on WD at 8 weeks of age for a total of 9 weeks (**Figure 3.2A**).

ORO staining on en face-prepared aortae illustrated that IRE1α-MacKO exhibited less lesion development in the abdominal aorta regions compared to those of WT mice (**Figure 3.2B**). Quantification of ORO+ lesions throughout the aorta revealed a significant reduction in plaque expansion in IRE1α-MacKO compared to WT (**Figure 3.2D**). Additionally, ORO staining of aortic root sections (**Figure 3.2C**) demonstrated that IRE1α-MacKO mice had significantly reduced plaque area compared to WT (**Figure 3.2E**). Together, ORO staining of both en face aortae and aortic root sections indicated that the deletion of IRE1α prevents plaque expansion.

To explore the cellular composition of the plaque, we performed immunofluorescence staining of the aortic root sections (**Figure 3.2C**). We saw that CD68+ area did not differ between the genotypes (**Figure 3.2F**), implying there was no change in the number of phagocytic macrophages when IRE1α was perturbed. However, αSMA+ area was significantly reduced in the aortic root sections of IRE1α-MacKO mice (**Figure 3.2G**), suggesting that the reduced plaque area could be attributed to a reduction in the VSMC population.

In the development of plaques, VSMCs undergo substantial proliferation and infiltrate into the intimal layers[92]. Therefore, we hypothesized that IRE1α-MacKO possessed fewer proliferating VSMCs, contributing to a reduction in the VSMC population and plaque area. To test this hypothesis, we also performed immunofluorescence staining using anti-Ki67 antibody to detect proliferating cells (**Figure 3.2C**). We observed that proliferating cells are significantly decreased in the IRE1α-MacKO when compared to those in WT animals (**Figure 3.2H**). To quantify proliferating VSMC populations, we measured the percentage of αSMA+ area that was also Ki67+. Although we saw an overall reduction of proliferating VSMCs in the IRE1α-MacKO mice, the reduction was not statistically significant due to an outlier in the group (**Figure 3.2I**).

To further explore the immune cell composition of the aorta, with a specific focus on the two cell types that drive atherosclerosis progression (macrophages and T cells), we digested whole aortas isolated from triple transgenic WT and IRE1α-MacKO mice into single-cell suspension and performed flow cytometry analysis. We found that macrophage (CD64+CD45+) and T cell (CD3+CD45+) populations were comparable between genotypes (**Figure 3.2J**), implying that the deletion of IRE1α in macrophages may not impact the recruitment or proliferation of these two populations. In addition, we looked at the inflammatory M1 (CD11b+) and anti-inflammatory M2 (CD206+) subsets

of macrophages, and we also found no differences between genotypes (**Figure 3.2J**). Lastly, helper T cell (CD4+) and cytotoxic/killer T cell (CD8+) populations were also comparable between the two genotypes (**Figure 3.2J**). Overall, we concluded that the deletion of IRE1α in myeloid cells did not impact the immune cell composition in the aorta.

The reduction in plaque area could result from improved local vascular homeostasis, conferred by both deleting IRE1α in vascular-residing macrophages and deleting IRE1α in myeloid cells residing in other organs. The liver, a pivotal organ in producing lipoproteins and regulating circulating cholesterol levels, may contribute to the anti-atherosclerotic phenotype through IRE1α perturbation in hepatic myeloid cells. Therefore, we measured the total cholesterol levels in the serums after a 6-hour fast. Interestingly, we found a significant reduction of cholesterol in male IRE1α-MacKO mice compared to that of male WT mice, suggesting that the reduced plaque area might result from improved hypercholesterolemia (**Figure 3.2K**). However, this difference was not observed in female mice, in which fasting cholesterol levels were grossly lower than in males.

In conclusion, the triple transgenic IRE1α-MacKO mice exhibited reduced plaque expansion in both en face aortae and aortic root sections compared to WT. Although macrophage and immune cell populations remained unchanged, there was a significant reduction in VSMCs in aortic root sections. Notably, there was an overall decrease in cellular proliferation in the IRE1α-MacKO aortic roots. Lastly, male IRE1α-MacKO mice displayed lower fasting cholesterol levels compared to that of WT control animals, potentially contributing to the observed improvement in atherosclerosis phenotypes.

DISCUSSION

This chapter investigates the impact of myeloid-specific IRE1α deletion on atherosclerosis progression in two models: AAV8-PCSK9-dependent and the triple transgenic model. The findings indicate that myeloid-specific IRE1α deletion prevents atherosclerosis progression by reducing overall plaque area. In the AAV8-PCSK9 model, extensive obesity may independently drive plaque development, potentially masking the protective phenotype in IRE1α-MacKO mice, as suggested by the correlation between plaque area and body weight. This protective effect appears more pronounced in lean IRE1α-MacKO mice during the early stages of atherosclerosis. To address potential cage effects on weight gain, single housing may be considered.

The triple transgenic model eliminates the possibility of a differential viral infection rate in the AAV8-PCSK9 model, which could confound the readouts. Notably, the triple transgenic model consistently supports the protective phenotype associated with myeloid-specific IRE1α deletion. The en face and aortic root ORO staining demonstrated reduced plaque expansion in KO mice. Moreover, alterations in cellular composition were evident, with IRE1α-MacKO mice exhibiting significantly fewer VSMCs and reduced cellular proliferation, indicative of plaque regression. Our flow cytometry-based analysis of the immune cell composition of the aorta also indicated that

the macrophage and T cell subpopulations remained unchanged in IRE1α-MacKO aortae. In recent years, single-cell transcriptomic studies have revealed the heterogeneity of vascular macrophage subsets beyond the canonical "M1" and "M2" classification[100]. Therefore, by incorporating recently identified markers, we can further elucidate macrophage subsets, such as resident (LYVE1^{high}), inflammatory (TLR2^{high}), and phagocytic (TREM2^{high}) macrophages. The total cholesterol assay on fasting serum demonstrated that IRE1α deletion in myeloid cells improves hypercholesterolemia, potentially ameliorating plaque pathogenesis by reducing LDL levels in the intima. To test the direct effect of macrophages on VSMCs, we plan to co-culture BMDMs from WT or IRE1α-MacKO mice with VSMCs (immortalized or primary preparations) in lipid-rich (SFAs and cholesterol) condition media and measure gene expression of VSMC proliferation and activation. A few studies have revealed that IL-1β signaling is involved in VSMCs migration[101] and proliferation, as well as inducing endothelial cells to secrete adhesion molecules that lead to immune cell infiltration[102,103]. Taken together, our studies demonstrate that targeting myeloid IRE1α confers protection against atherosclerosis and restores stable cellular composition in the vasculature.

MATERIALS & METHODS

Mouse Studies

AAV8-PCSK9 mouse model of atherosclerosis

AAV8-mPCSK9 with gain-of-function mutation (D377Y) was purchased from Vector Biolabs and diluted with PBS (-CaCl2,-MgCl2) for injection. IRE1α myeloid-knockout mice (IRE1α-MacKO) were injected with AAV8-mPCSK9 at the titer of 2E11 GC in 100uL through tail veins at age of 8 weeks. At the age of 9 weeks, the mice were placed on the western diet (TD.88137, ENVIGO) for 13 weeks to develop atherosclerotic lesions.

Myeloid-specific IRE1α KO model of atherosclerosis (triple transgenic)

IRE1α myeloid-KO mice (LysM-Cre, IRE1α$^{f/f)}$ were crossed into Ldlr$^{-/-}$ proatherogenic background (B6.129S7-Ldlrtm1Her/J, The Jackson lab, cat# 002207). The mice were placed on the western diet (TD.88137, ENVIGO) for 9-10 weeks to develop atherosclerotic lesions All procedures were performed in accordance with protocols approved by the Institutional Animal Care and Use Committee at the University of California, San Francisco. Animals were kept in a specific pathogen-free animal facility on a 12 hr light- dark cycle at an ambient temperature of 21°C. They were given free access to water and food.

Aortic Tissue Processing, ORO Staining, and Analysis.

Mice were sacrificed and perfused with PBS + Heparin (2000U/mL) at the end of the dietary regimen. Top 1/3 of the heart (aortic root) was cryopreserved and sectioned at 10um thickness. The appearance of the sinus of three leaflets of aortic valves is an indicator of a successful section of the aortic root.

The sections were air-dried at room temperature for 30 minutes, fixed in 10% neutral buffered formalin for 10 minutes, and stained with Oil Red O (ORO) 0.5% solution followed by Mayer's hematoxylin staining (as described in chapter 2). Keyence BZ-X700

was used for brightfield image acquisition. Lesion areas were quantified by measuring the ORO+ area using ImageJ from 4 serial sections per mouse.
To prepare en face aorta ORO staining, the whole aortae were fixed in 10% formalin overnight, longitudinally cut open, and stored in PBS. 0.5% ORO solution is used for staining. After overnight washing with propylene glycol, aortae were pinned down on silicone elastomer coated dishes using insect pins. Images were taken using a brightfield micro-dissection microscope. The lesion areas were quantified by calculating the ORO+ area out of total vessel area.

Immunofluorescence Staining & Imaging
Antibody buffer (pH 7.4): 200ml deionized water, 2.25g NaCl, 1.5g Tris base, 2.0g BSA, 3.6g L-Lysine, 2mL 4% Azide in water, 0.3% TritonX.
Permeabilization solution: 0.1% Triton X–100, 0.1% sodium citrate, freshly prepared.
Blocking buffer: 10% donkey serum, 90% antibody buffer, 0.3% Triton X

OCT-embedded sections were air-dried and fixed in 4% PFA for 20 min at RT and washed with PBS. Permeabilize sections for 2 min at 4°C and wash with PBS. Block for 1 hour at RT and stain with primary antibodies over night at 4°C in a humidified chamber. All immunofluoresence antibodies are listed in **Table 3.1**. Next day, wash off the primary antibody with PBS (10 min x 3), and incubate with secondary antibodies for 1 hour at RT. Wash off the secondary antibodies with PBS (10 min x 3). Mount with mounting media with DAPI (VectorShield). Images were taken with Keyence BZ-X700.

Aorta Digestion into Single-Cell Suspension
Isolate aorta after perfusion and digest in 2.5ml of aortic adventitia digestion enzyme solution (AADES) [312.5 U/ml Collagenase II (Worthington, LS004176), 5.6248 U/ml Elastase I (Worthington, LS0022920), dissolve in RPMI (10% heat-inactivated FBS)] at 37°C for 10 min. Replace AADES with RPMI, and peel off adventitia from aorta. Cut the rest of aorta into small pieces and digestion in aorta dissociation enzyme solution (ADES) [125 U/ml Collagenase Type XI (Sigma, C7657), 60 U/ml Hyaluronidase type 1-s (Sigma, H3506), 60U/ml DNase I (Roche, 1010415900), 450 U/ml Collagenase type I (Alfa Aesar, J62406), dissolve in 2.5mL of RPMI (10% heat-inactivated FBS)] for 1 hour at 37°C. Pass digested sample through 70um cell strainer into 5mL FACS tubes. Quench digestion with 2mL of RPMI by passing it through filter cap to flush off remaining cells. Centrifuged samples 5 min at 500 x g at 4°C and discarded supernatant. Resuspend the cell pellet with 1mL of RPMI and count the cells. Centrifuged samples 5 min at 500 RCF at 4°C and discarded supernatant.

Flow Cytometry
Make FACS buffer (10% heat-inactivated FBS, 2mM EDTA) with FC Block (1:200) and make master mix by adding conjugated-antibodies to the FACS buffer. Stain the cell by adding 300-400uL master mix to each sample. All flow antibodies are listed in **Table 3.2**. Vortex to mix and incubate in the dark for 30 min at 4°C. Centrifuged samples 5 min at 500 x g at 4°C and discarded supernatant. Wash by adding 3 mL of FACS buffer and centrifuge samples 5 min at 500 x g at 4°C and discarded supernatant. Stain with DAPI

at final concentration 0.25ug/mL as viability stain. Flow cytometry machine used is BD *LSRII* Cell Analyzer at the UCSF Flow Cytometry Core.

Cholesterol Assay

Mice were fasted for total 6 hour before blood collection. Serum was prepared by centrifuging blood samples at 1,200 x g for 10 minutes. The total cholesterol was measured by using Cholesterol E Kit (FUJIFILM, 999-02601) following manufacturer's protocol.

Statistical Analysis

All statistical analyses were performed using GraphPad Prism version 8.1 software. Student's t test or two-way ANOVA were applied to determine statistical difference between two groups. Data are presented as mean ± SEM. Significance was defined by a p value < 0.05. p values: * < 0.05; ** < 0.01; *** < 0.001; NS, non-significant.

TABLE 3. 1 Immunofluorescence antibody list

Antibody	Source & Catalog #	Dilution
Mouse anti-aSMA	Bio-Rad, MCA5781GA	1:200
Rat anti-CD68	Bio-Rad, MCA1957	1:200
Rabbit anti-Ki67	Abcam, ab16667	1:200
Alexa 488 Donkey anti-rat	Invitrogen, A-21208	1:500
Alexa 555 Donkey anti-mouse	Invitrogen, cat # A-31570	1:500
Alexa 647 Donkey anti-rabbit	Invitrogen, cat # A-31573	1:500

TABLE 3. 2 Flow cytometry antibody list

Antibody	Source & Catalog #	Dilution
CD45.1-BV605	BioLegend, 110737	1:400
CD64-PE	BioLegend, 161003	1:500
CD11c-BV785	BioLegend, 117335	1:600
CD206-PerCP/Cy5.5	BioLegend, 141715	1:1000
CD3-PE Cyanine7	BioLegend, 100219	1:400
CD4-FITC	BioLegend, 100405	1:800
CD8-APC	BioLegend, 100711	1:400

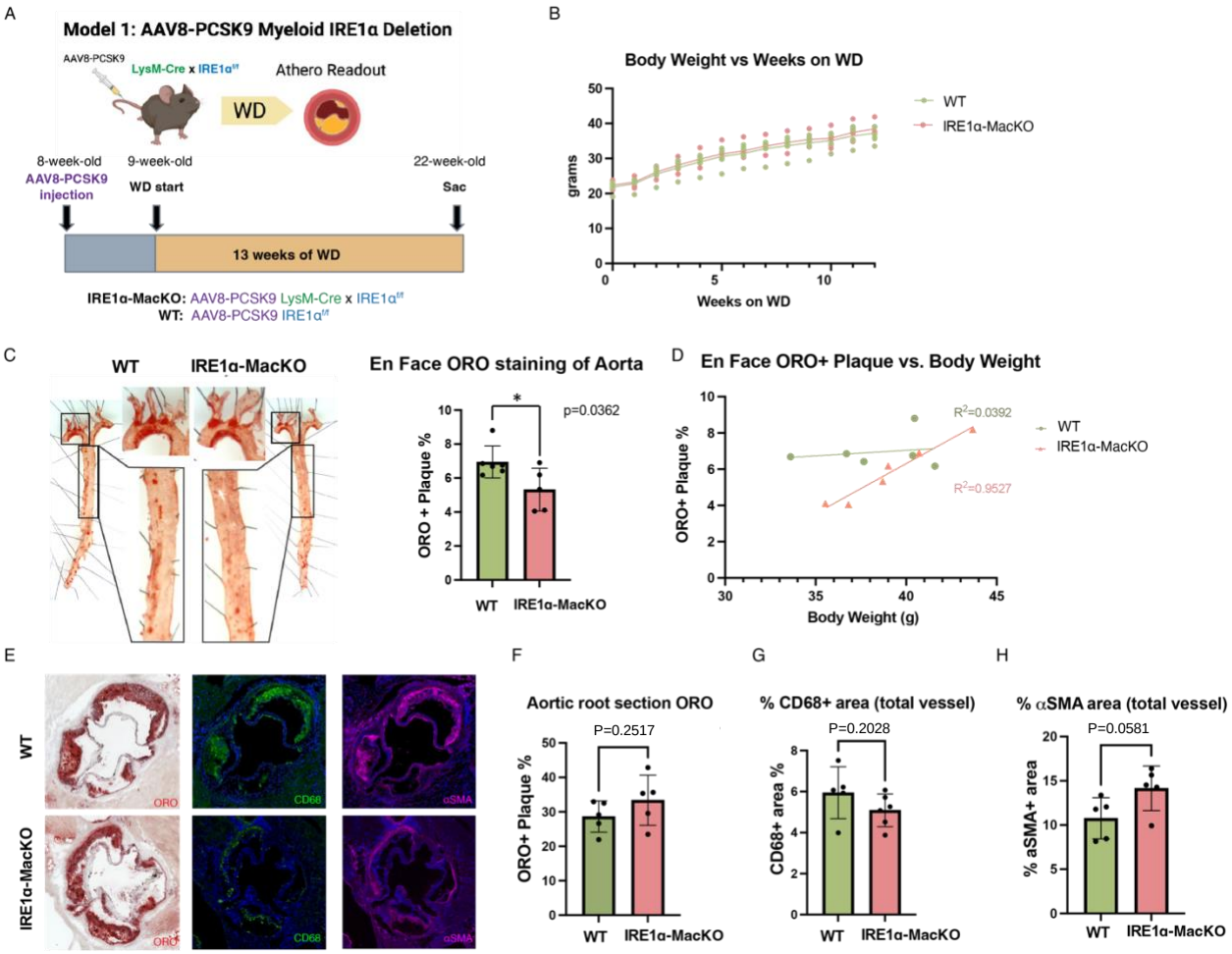

FIGURE 3. 1 AAV8-PCSK9 myeloid-Specific IRE1α deletion mice displayed overall reduction in plaque development.

A) Schematic of AAV8-PCSK9 induced atherosclerotic mouse model of WT and IRE1α-MacKO mice. **B)** Body weight curve over the course of first 12 weeks on western diet. **C)** En face ORO staining of aorta and ORO+ lesion quantification from both WT and IRE1α-MacKO mice after 13 weeks of WD. **D)** Correlation analysis of ORO+ lesion area percentage vs. body weights. **E)** ORO and immunofluorescence staining of aortic root. CD68 (macrophages); αSMA (VSMCs). **F-H)** Quantification of ORO+ lesion (F), CD68+ macrophage (G), and αSMA+ VSMC (H) area over total vessel area. Two-tail T test were performed (* < 0.05)

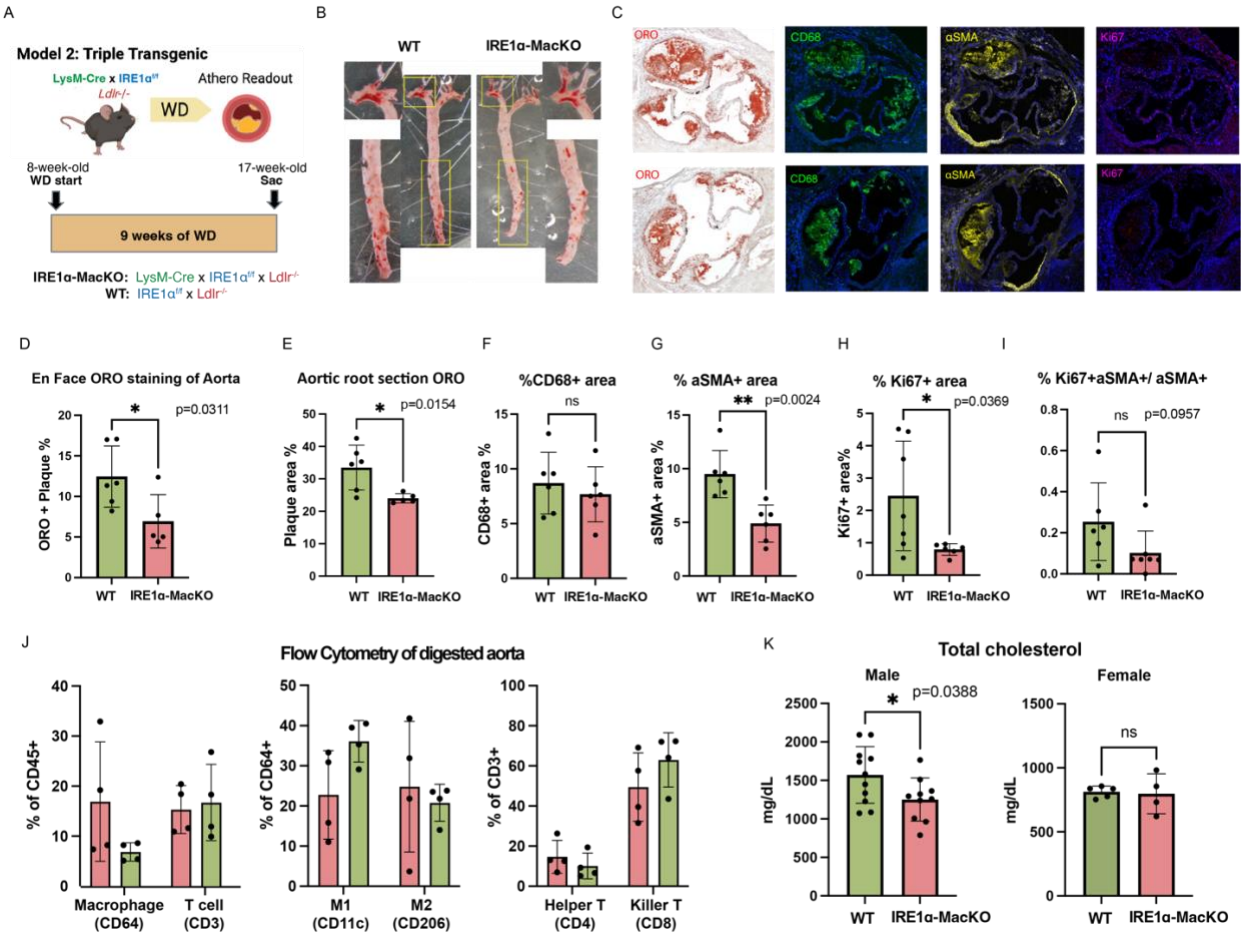

FIGURE 3. 2 Triple transgenic myeloid-specific IRE1α deletion mice showed reduction in plaque development, VSMC population and vascular proliferation.

A) Schematic of triple transgenic IRE1α-MacKO mice. **B)** En face ORO staining of aorta and ORO+ lesion quantification from both WT and IRE1α-MacKO mice after 9 weeks of WD. **C)** ORO and immunofluorescence staining of aortic root. CD68 (macrophages); αSMA (VSMCs); proliferating cells (Ki67). **D)** Quantification of en face ORO staining. **E-H)** quantification of ORO+ lesion (E), CD68+ macrophage (F), αSMA+ VSMC(G) and Ki67+(H) proliferation area over total vessel area. **I)** Quantification of proliferating VSMC area over total VSMC area. **J)** Flow cytometry analysis of digested aorta. **K)** Total cholesterol assay on serum collected from mice after 6-hour fasting. Two-tail T test were performed.

CHAPTER 4

Structural Functional Characterization of IRE1α Stress-Sensing Mutants

ABSTRACT

IRE1α is an essential ER stress sensor, and its structure is highly evolutionarily conserved across different organisms. Recent studies in yeast and mammalian cells unveiled that the transmembrane (TM) domain of IRE1α is able to sense lipid-bilayer stress upon ER membrane lipid saturation. These data provide a mechanistic explanation to our previous observation: SFA-induced IRE1α activation is dependent on SFA incorporation into membrane phospholipids. Most importantly, our transcriptional analysis of SFA-treated macrophages showed an enrichment of target genes under the adaptive UPR rather than the terminal UPR, which is driven by unfolded protein stress. These data indicated that macrophage IRE1α can sense both protein and lipid stress through separate structural elements, and each elicits differential downstream transcriptional signatures. In this chapter, we employed a CRISPR-based approach for genetic editing, generating IRE1α mutant macrophage cell lines harboring different structural and functional mutations. We successfully generated and validated an IRE1α knockout macrophage cell line, demonstrating the feasibility of our homology-directed repair template design by identifying mutant cells within the CRISPR-edited pools.

INTRODUCTION

IRE1α is ubiquitously present in eukaryotes, with orthologs identified across diverse organisms, underscoring its evolutionary conservation[104–107]. The IRE1α protein encompasses three distinct domains: the luminal domain (LD), TM, and cytosolic domain. The LD, normally interacting with the BiP chaperone, serves as a sentinel for unfolded and misfolded protein stress within the endoplasmic reticulum (ER) lumen. Under stress conditions, BiP dissociates, enabling LD dimerization, and ultimately initiates IRE1α activation[12,108–110]. Intriguingly, the TM domain of IRE1α was shown to harbor a lipid-sensing function which, upon ER membrane saturation, activates IRE1α independently of its ER luminal domain[8,9,111]. Cho et al. specifically demonstrated that transmembrane residues S450 and W457 mediate dimerization in human IRE1α protein following treatment with SFAs[8]. Notably, the deletion of the LD did not impede SFA-induced IRE1α activation[8]. This pivotal discovery suggests that the structural element responsible for IRE1α activation by lipid stress is distinct from that governing its responsiveness to unfolded or misfolded proteins.

Early investigations from our laboratory revealed that a 20-hour treatment with SFAs selectively induces an adaptive UPR signature in macrophages rather than that of the terminal UPR[21], suggesting that SFA-induced IRE1α activation elicits a distinct stress response modality from that of the canonical UPR. Additionally, our studies demonstrated that pharmacological inhibition of phospholipid biosynthesis abolished XBP1 splicing activity and significantly diminished IL-1β production, indicating that SFA-induced IRE1α activation is contingent upon phospholipid saturation[21]. Collectively, our prior research supports the concept that IRE1α serves as a sensor of lipid stress, underscoring its multifaceted role in cellular homeostasis.

We hypothesize that disrupting the putative lipid-sensing function of IRE1α by targeting its TM domain would be sufficient to abrogate the ability of macrophages to undergo SFA-induced inflammatory activation. My collaborating team at the UCSF Cell and Genome Engineering Core and I have developed CRISPR-based approach to mutagenize the TM domain and LD of IRE1α in a macrophage model, allowing us to interrogate the role of these domains in the context of lipid- and protein-driven macrophage activation.

RESULTS

IRE1α functional KO in mouse immortalized bone marrow-derived macrophages abrogated stress-induced Xbp1 splicing activity and diminished inflammatory response

The IRE1α protein in both humans and mice consists of a total of 977 amino acids and is encoded by 22 exons. For the generation of a functional KO cell line, we opted to target exons 2-11, encompassing a significant portion of the luminal domain (**Figure 4.1A**). Utilizing two guide RNAs (gRNAs) with established high editing efficiency in mouse embryonic stem cells, we performed electroporation of gRNA-Cas9 ribonucleoproteins (RNPs) in mouse immortalized BMDM (iBMDM) using the Lonza™ Nucleofector system or a control plasmid expressing green fluorescent protein (GFP). After electroporation, the edited cell pool was recovered and expanded. Single-cell-derived clones were subjected to genotyping through targeted site PCR to detect the presence of mutant DNA sequences. Clones positive for mutations were further confirmed by sequencing to ensure accurate editing had taken place (**Figure 4.1B**).

We identified four clones (10.43, 20.30, 20.34, and 20.38) through genotyping: 10.43 and 20.30 were found to be homozygous for the mutant alleles, while 20.34 and 20.38 were heterozygous. Subsequently, we conducted western blot analysis on these clones, along with WT cells, using an anti-IRE1α antibody targeting the cytosolic epitope. Cells were subjected to either no treatment or administration of tunicamycin at 0.5 μg/mL for 16 hours (**Figure 4.1C**). The heterozygous clones (20.34 and 20.38) exhibited bands characteristic of WT IRE1α, with no discernible evidence of the mutant band. Interestingly, the homozygous KO clones (10.43 and 20.30) displayed a faint mutant band (**Figure 4.1C**). One plausible explanation is that in the presence of both WT and mutant alleles, the cells tend to preferentially express WT IRE1α. The absence of a mutant band in heterozygous clones could be attributed to potential degradation of the mutant IRE1α protein. Conversely, in the case of homozygous clones where no WT protein is present, the cells might be compensating by upregulating IRE1α to a level that surpasses the rate of degradation, enabling the detection of the mutant protein. Upon tunicamycin treatment, which induces UPR and upregulates ER stress sensors like IRE1α, we noted an increase in WT IRE1α protein in the WT cells (**Figure 4.1C**). Importantly, the intensity of the mutant band also increased in the homozygous clones following tunicamycin treatment, while no such increase was observed in the heterozygous clones. The observed dynamics in band intensity suggest a regulatory mechanism influenced by the cellular presence of WT and mutant alleles in response to IRE1α expression. In addition, we performed immunofluorescence staining using anti-

IRE1α antibody and found that, despite loss of functionality, 20.30 had strong IRE1α signals, confirming that mutant IRE1α was expressed (**Figure 4.1D**).

To confirm the functionality of IRE1α is completed knocked out, we performed the XBP1 splicing assay on clones under different stress stimuli. We first treated clones with tunicamycin and found that heterozygous clones had reduced splicing activity (73.5% & 69.5%) compared to WT (85.6%). Homozygous clone 10.43 displayed a significant reduction (23.6%) in response to tunicamycin, and clone 20.30's XBP1 splicing activity was completely abolished (7.3%) to the level of vehicle treatment (9.3%) (**Figure 4.1E**). This difference between the two homozygous lines were implicated in the western blot: 10.43 clone's mutant band was fainter than 20.30's, and with tunicamycin treatment, 10.43 had a faint band appeared at the molecular weight of WT, suggesting it may not be a completely homozygous mutant. Therefore, we decided to focus on homozygous clone 20.30 for further characterization.

We also performed the XBP1 splicing assay on cells treated with increasing doses of PA to induce lipid-stress and those co-treated with oleic acid (OA). We observed that PA-treated WT cells had increased splicing activity, and co-treatment with OA abolished the splicing activity. In contrast, 20.30 mutant clone did not respond to PA treatment at all, indicating its inability to senses lipid stress. Since the cytosolic domain of the mutant is still intact, the lack of stress responsiveness could be a result of perturbed stress-sensing ability (**Figure 4.1F**).

To further confirm that 20.30 is a true functional KO clone, we treated cells with thapsigargin, which induces ER stress by depleting ER calcium storage, and G-1749, a potent allosteric activator of IRE1α's RNase activity[112]. The WT cells responded to thapsigargin and G-1749 with elevated XBP1 splicing activity, but this response was completely abolished in 20.30 KO clones (**Figure 4.1F**). Lastly, we performed IL-1β ELISA on condition media collected from WT cells and 20.30 KO clone that were lipopolysaccharide(LPS)-primed prior to PA treatment. We found that 20.30 KO had significantly reduced IL-1β production compared to WT, confirming that 20.30 KO had dampened the downstream pro-inflammatory pathway (**Figure 4.1G**).

In conclusion, using a CRISPR-based approach, we generated and validated an IRE1α loss-of-function KO iBMDM cell line. Specifically, we showed that the KO cell line did not respond to unfolded protein stress or lipid stress and was not activated by the IRE1α allosteric activator. Moreover, the downstream IL-1β production was diminished in KO compared to the WT cells.

Successful mutant detection in CRISPR-based editing of IRE1α luminal domain deletion and transmembrane domain mutation

SFAs, once taken up by macrophages, flux rapidly into phospholipids that are known to comprise membranes of organelles including the ER[21]. Human IRE1α TM residues Trp457 and Ser450 were shown to be essential for IRE1α dimerization in response to SFA stress[8]**.** We designed a TM mutant iBMDM cell line with disabled lipid-sensing function by introducing point mutations at the two critical residues and a LD deletion

(ΔLD) cell line with disabled unfolded protein-sensing function (**Figure 4.2A**). We expected the TM mutant macrophages to be protected against lipid-induced UPR, XBP1 splicing, and inflammatory activation such as NLRP3 inflammasome activation. However, TM mutant macrophages should still engage the UPR in response to tunicamycin and other unfolded protein stress inducer. In contrast, ΔLD macrophages should be resistant to tunicamycin but still responsive to SFAs. We designed CRISPR knock-in strategies to generate these cell lines by electroporating Cas9-gRNA RNA with homology-directed repair templates for introducing the desired mutations.

To generate a TM mutant macrophage cell line, we initially performed a protein sequence alignment of the human TM domain and the mouse TM domain. We observed a complete conservation in the TM domain, with critical lipid-sensing residues identified as S452 and W459 in mouse IRE1α (**Figure 4.2 B**). To introduce point mutations, we validated a gRNA targeting the intron following exon 12 where the TM domain (446-466 aa) is located. The cDNA repair template was designed to encode exon 12 with S452A and W459A mutations. To enrich for edited cells, we included a neomycin resistance gene in the anti-strand under the PGK promoter, along with its own stop codon (**Figure 4.2C**). This design does not interfere with IRE1α expression but aided in selecting cells that successfully incorporated the knock-in (KI) sequences. Additionally, we incorporated a 1000bp long homology arm (HA) with a sequence matching the regions of introns flanking exon 12. Employing a similar approach for generating the IRE1α functional KO cell line, we electroporated Cas9-gRNA RNP and a repair template (GFP-expressing plasmid alone as a control) into iBMDM cells. Following electroporation, we performed neomycin selection and expanded the surviving pools. Due to challenges in finding suitable primers for site-directed PCR, we opted to conduct a functional assay to test whether these pools behave as expected. We treated both WT and edited pools with thapsigargin for unfolded protein stress and PA as lipid stress for an XBP1 splicing assay (**Figure 4.2 D**). One of the edited pools exhibited significantly diminished XBP1 splicing activity in response to PA treatment (11.8% and 14.7%) compared to WT (97.1% and 96.9%). Interestingly, its responsiveness to thapsigargin (21.0% and 17.2%) was comparable to that of WT (27.0% and 26.2%). This data indicates that this TM-edited pool has abolished the IREα lipid-sensing function, while the protein-sensing function remains unimpaired.

The human IRE1α LD consists of residues 30-407 aa, while the corresponding mouse LD residues are 32-409 aa based on our protein alignment analysis. To generate the ΔLD mutant, we employed a previously validated gRNA targeting intronic sequences before exon 2 to create a double-strand cut site. The cDNA repair template comprised sequences encoding the ΔLD residues after Exon 1 (21-31 aa + 410-977 aa) followed by a stop codon and an SV40 polyA signal. To ensure proper pre-mRNA splicing, we added 200bp intronic sequences from the intron-exon boundary of exon 2 (**Figure 4.2 E**). This ensures that the knocked-in sequences inserted in the intronic region will not be spliced out during mRNA maturation. Additionally, we added a 1000bp-long HA that match the region of the gRNA target site to both ends of the repair template. After electroporation, we expanded the edited pools and genotyped them by site-directed PCR. The sequenced PCR product confirmed that three pools had detectable

sequences indicating the presence of proper editing. Subsequently, we performed a western blot and found that all three edited pools (4a, 4b, and 4c) exhibited strong WT IRE1α bands (~110kD) and faint bands (~60kD) representing the ΔLD mutant IRE1α (**Figure 4.2 F**). As expected, this mutant band was absent in the WT cells. These data indicate successful homology-based editing, and the edited cells were present in the electroporated pools.

In conclusion, we have demonstrated the feasibility of our CRISPR-based approach to generate ΔLD and TM mutant iBMDM cell lines. The presence of the ΔLD mutant IRE1α protein was detectable in the edited pools, and the TM mutant pool was functionally validated. Our next step will involve generating single-cell-derived clones from these pools and conducting both sequence and functional characterizations.

DISCUSSION

This chapter demonstrates the feasibility of using a CRISPR-based approach to generate IRE1α KO, ΔLD, and TM mutant cell lines. One advantage of this genomic editing approach, as opposed to overexpressing mutant constructs on a KO background, is that it physiologically resembles the endogenous expression level and stability of IRE1α protein. While previous studies have successfully expressed IRE1α mutant constructs in various cell lines, including HEK293T, mouse embryonic fibroblasts, and INS-1 rat insulinoma cells, none have precisely perturbed IRE1α structural elements in macrophage cell lines[23,110]. Our IRE1α mutant macrophage cell lines will enable us to distinguish the nuances between lipid-induced and unfolded protein-induced IRE1α activation, as well as their impact on downstream inflammatory pathways.

Moreover, our construct design can be easily modified for IRE1α mutant mouse line generation. Taking ΔLD as an example, we can reverse the cDNA repair template sequence and insert "FLEx-switch" LoxP sites at both ends of the KI template. This modification will allow ΔLD IRE1α to be expressed only in the presence of Cre recombinase, and only endogenous WT IRE1α will be expressed in the absence of the enzyme. With this construct, we can investigate the pathological relevance of tissue-specific IRE1α protein-sensing perturbations.

MATERIALS & METHODS

Cell line

The immortalized bone marrow derived macrophages cell lines were a gift from Dr. Susan Carpenter’s lab at UC Santa Cruz. BMDMs were immortalized using J2 virus[113]. gRAN targeting efficiency were tested in mESCs.

Electroporation

P3 primary cell 96-well Nucleofector kit (Lonza, V4XP-3032) and 4D-Nucleofector system was used for electroporation. Single-guide RNAs were hybridized by mixing crRNA (**TABLE 4.1**) and tracrRNA (resuspended in IDTE solution) at 95°C for 5 minutes, followed by cooling to RT. Prepare sgRNA-Cas9 RNP by mixing sgRNA (3uL) and IDT Cas9p (2uL) in PBS per sample and incubate at RT for 10-20 minutes. Mix Nucleofector kit solution with provided supplement (total 20uL per sample). Add 2.5E5 iBMDM cells resuspended in 20ul Nucleofector kit solution with supplement into each RNP and DNA aliquot. Add total of 1ug of ΔLD or TM donor cDNA and 5ul of sgRNA-Cas9 RNP to each sample. Control samples included pMasx-GFP only, ΔLD RNP alone, and TM RNP alone control samples. Electroporate using ZAP program DN100. Immediately add 80u of DMEM,10%FBS, 1% PS to each Nucleocuvette an gently transfer to 96-well plate well containing 175uL media. Check GFP signal next day to check for success electroporation.

Genotyping
After expanding the cells and neomycin selection 500ug/mL in TM pools, genomic DNA was isolated for PCR and gel electrophoresis. The primers used are listed in **Table 4.2**. The PCR protocol followed the Q5 high-fidelity DNA polymerase (New England BioLabs, M0491) manufacture instruction.

Western blot & XBP1 Splicing Assay.
See Materials & Methods section in Chapter 1.

Immunofluorescence Staining
WT and mutant cells were plated onto 8-chamber slides (Lab-Tek Chamber slides, Cat. #177402) to 50-70% confluency. Cells were washed 2x with PBS and fixed with 4% PFA for 15 mins inside of chambers. Apply permeabilization solution/90.1% Triton X–100, 0.1% sodium citrate, freshly prepared) at 4°C for 2 min and washed with PBS. Apply blocking buffer (10% donkey serum, 90% antibody buffer, 0.3% Triton X) and incubate for 1 hour at RT. Apply Rabbit anti-human IRE1α antibody (NOVUS, NB100-2324) at 1:200 dilution and incubate at 4°C overnight. The next day, wash off primary antibody 3x 10min with PBS and apply Donkey anti-Rabbit IgG (H+L), Alexa Fluor 488 (Thermo Fisher, A-21206) at 1:1000 dilution in antibody buffer and incubate at RT for 1 hour. The secondary antibody was washed off with PBS 10 minutes x 3. Mount with mounting media with DAPI (VectorShield). Images were taken by Leica SP8 LSM White Light Laser confocal microscope at 63 x magnification (equipment provided by Biological Imaging Development Colab, UCSF)

IL-1β ELISA Assay
Cells were primed with LPS at 200 ng/mL for 3 hours, followed by treatment with PA/BSA for 16 hours. Conditioned media were collected after the 16-hour treatment, centrifuged at 1000 x g, and the supernatant was collected. Samples were stored at -80 °C for long-term storage. The Mouse IL-1 beta/IL-1F2 DuoSet ELISA kit (Biotechne, R&D SYSTEM, Cat. #: DY401) was used according to the manufacturer's protocol.

TABLE 4. 1 List of gRNAs

crRNA	Sequence	Editing efficiency (% INDEL)
LD g7 (KO & ΔLD)	TAGCTGCTGGAGTTGAGCTA	27%
LD g1 (KO)	GTTCTAAAATCTCTGAACAA	24%
TM g3r	AGAGGAGTACCAGAACTTGG	94%

TABLE 4. 2 List of primers used for genotyping

Primer	Forward	Reverse	Mutant band size (bp)
KO	GTCTTGAGCCACCATGCAGT	TGAGATGGAGGGGTCAGGAT	3760
TM	ACATGGCTTCTCTCGAGTGC	CGTCAGCAGGTCTCACTCC	912
ΔLD	CCAGCACCAACAGTTCCAGA	AGGTGGGCAAAGTCCTTCTG	555

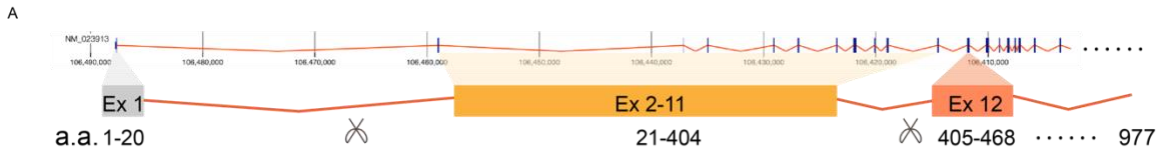
A
NM_023913
Ex 1
Ex 2-11
Ex 12
a.a. 1-20
21-404
405-468 ····· 977

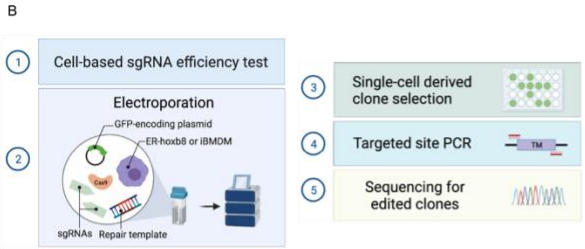
B
1 Cell-based sgRNA efficiency test
2 Electroporation
GFP-encoding plasmid
ER-hoxb8 or iBMDM
sgRNAs
Repair template
3 Single-cell derived clone selection
4 Targeted site PCR
5 Sequencing for edited clones

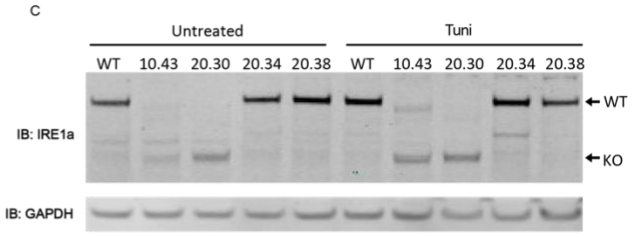
C
Untreated
Tuni
WT 10.43 20.30 20.34 20.38 WT 10.43 20.30 20.34 20.38
IB: IRE1a
WT
KO
IB: GAPDH

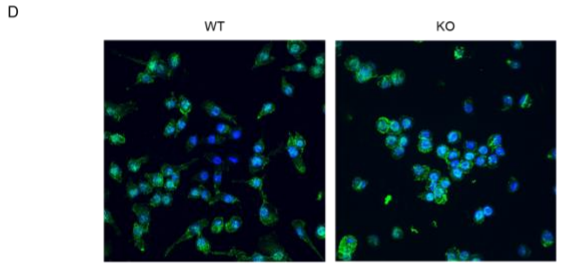
D
WT
KO

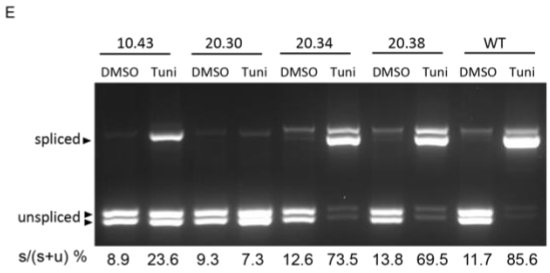
E
10.43 20.30 20.34 20.38 WT
DMSO Tuni DMSO Tuni DMSO Tuni DMSO Tuni DMSO Tuni
spliced
unspliced
s/(s+u) % 8.9 23.6 9.3 7.3 12.6 73.5 13.8 69.5 11.7 85.6

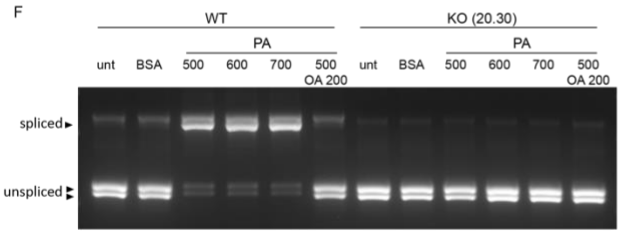
F
WT
KO (20.30)
PA
unt BSA 500 600 700 500 OA 200
spliced
unspliced

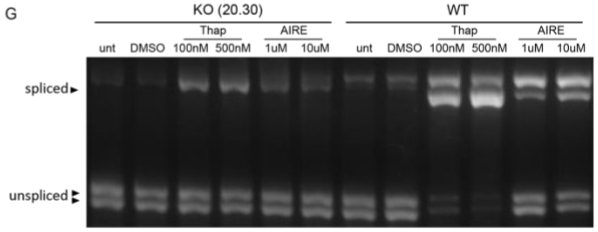
G
KO (20.30)
WT
Thap
AIRE
unt DMSO 100nM 500nM 1uM 10uM
spliced
unspliced

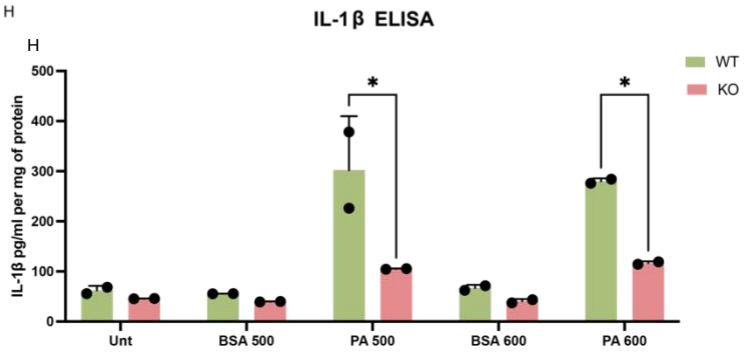
H
IL-1β ELISA
H
IL-1β pg/ml per mg of protein
500
400
300
200
100
0
WT
KO
*
*
Unt
BSA 500
PA 500
BSA 600
PA 600

FIGURE 4. 1 Validation of CRISPR-based IRE1α knock-out in immortalized bone marrow-derived macrophage (iBMDM) cell line.

A) Design of CRISPR-based IRE1α KO. Exons 1-19 are represented as navy blue bars. Introns are represented as red lines in between. Exon 1-12 and the amino acids encoded were annotated below. Two gRNAs targeting intronic sequences between exon 1-2 and between exon 11-12 are represented as scissor symbols. **B)** Schematics of the workflow. **C)** Western blot of IRE1α proteins in WT, homozygous KO clones (10.43 & 20.30), heterozygous KO clones (20.34 & 20.38) iBMDM. The molecular weight of WT IRE1α and mutant IRE1α are 110kD and 61kD respectively. Tuni: 0.5ug/mL tunicamycin treatment for 8 hours. **D)** Immunofluorescence staining of IRE1α protein (green) and nucleus (DAPI, blue) on AT and 20.30 (homozygous KO) cell lines. **E)** Xbp1 splicing assay of homozygous mutants and heterozygous mutants treated with tunicamycin (0.5ug/mL) for 16 hours. Arrows indicate spliced and unspliced bands. **F)** Xbp1 splicing assay on WT and 20.30 were treated with palmitic acid (PA) at increasing dosage or co-treatment with oleic acid (OA) for 16 hours. Bovine serum albumin (BSA): vehicle for fatty acids treatment. **G)** Xbp1 splicing assay on 20.30 and WT cell lines that were treated with thapsigargin or DMSO for 8 hours. **H)** IL-1β ELISA on condition media collected from WT and 20.30 KO cell lines that were primed with LPS (200ng/mL) for 3 hours followed by PA or equal-volume BSA control treatment for 16 hours.

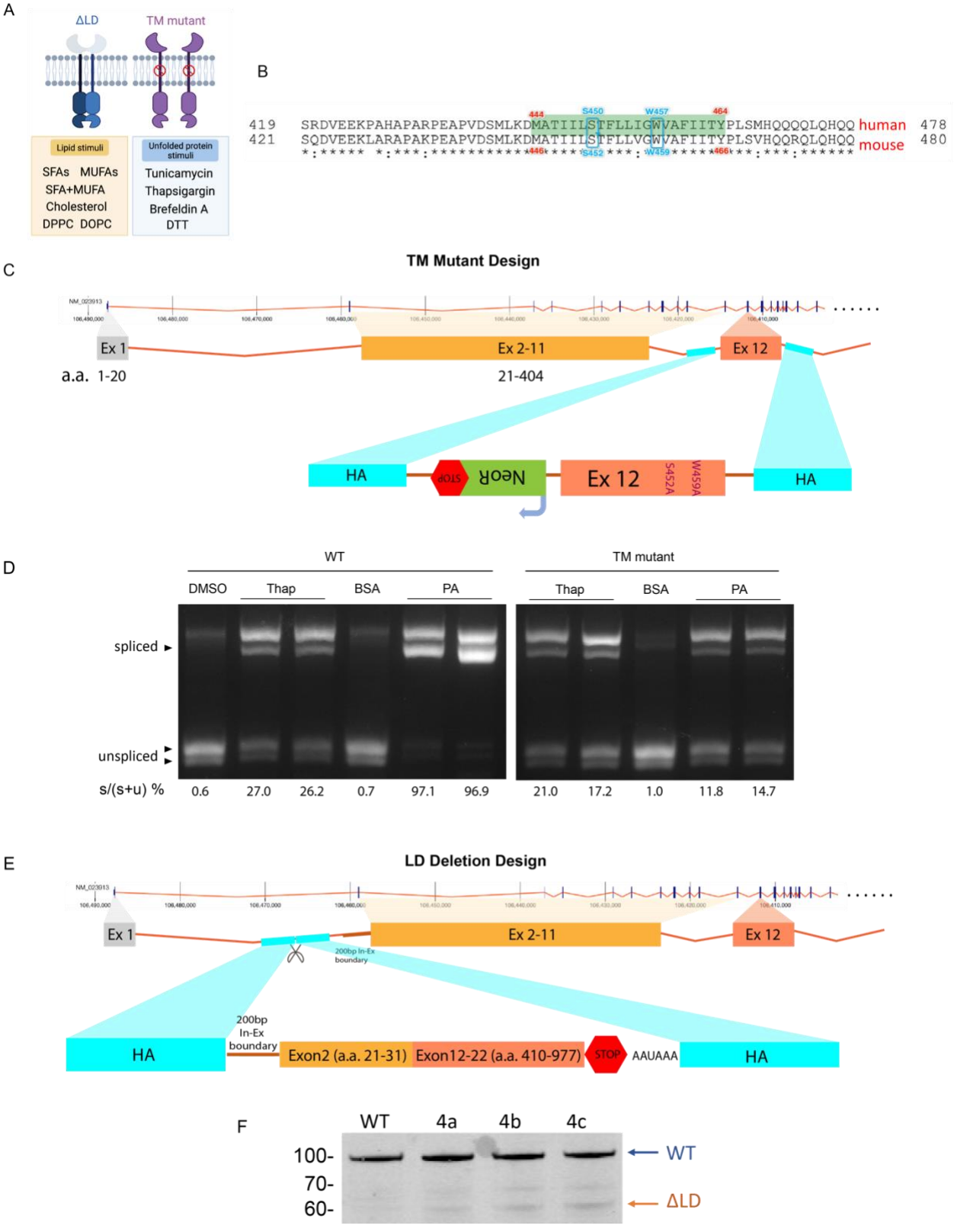
A
ΔLD
TM mutant
Lipid stimuli
SFAs MUFAs
SFA+MUFA
Cholesterol
DPPC DOPC
Unfolded protein stimuli
Tunicamycin
Thapsigargin
Brefeldin A
DTT
B
419 SRDVEEKPAHAPARPEAPVDSMLKDMATIILSTFLLIGWVAFIITYPLSMHQQQQLQHQQ human 478
421 SQDVEEKLARAPAKPEAPVDSMLKDMATIILSTFLLVGWVAFIITYPLSVHQQRQLQHQQ mouse 480
C
TM Mutant Design
Ex 1
Ex 2-11
Ex 12
a.a. 1-20
21-404
HA
NeoR
STOP
Ex 12
S452A
W459A
HA
D
WT
TM mutant
DMSO
Thap
BSA
PA
Thap
BSA
PA
spliced
unspliced
s/(s+u) %
0.6
27.0
26.2
0.7
97.1
96.9
21.0
17.2
1.0
11.8
14.7
E
LD Deletion Design
Ex 1
Ex 2-11
Ex 12
200bp In-Ex boundary
HA
200bp In-Ex boundary
Exon2 (a.a. 21-31)
Exon12-22 (a.a. 410-977)
STOP
AAUAAA
HA
F
WT
4a
4b
4c
100-
70-
60-
WT
ΔLD

FIGURE 4. 2 Generation of luminal domain deletion and transmembrane mutant iBMDM cell lines.

A) IRE1α ΔLD and TM mutant structural difference and predicted responsive stress inducer. SFAs: saturated fatty acids, MUFAs: mono-unsaturated fatty acids, DPPC: 1,2-dipalmitoyl-sn-glycero-3-phosphocholine, DOPC: 1,2-dioleoyl-sn-glycero-3-phosphocholine, DTT: dithiothreitol. **B)** Transmembrane domain protein sequence (highlighted in green) comparison between human vs mouse IRE1α. The lipid-sensing residues are marked in blue. **C)** TM mutant homology directed-repair cDNA template. Two mutated residues (S452A will W459A) coding sequences will be part of exon 12 repair template. In the intronic sequence before exon12, a neomycin-resistance gene is inserted in the reverse reading direction, driven by CAG promoter, and terminated by a stop codon. **D)** Xbp1 splicing assay on WT and one of the TM mutant pools from neomycin selection. Cells were treated with Thapsigargin (Thap, 100nM) and PA (500uM) for 8 hours. DMSO and BSA were vehicles for Thap and PA respectively. **F)** ΔLD homology-directed repair template cDNA design. HA: homology arm. Sequences encoding LD-truncated protein are showed as yellow and orange rectangles. STOP: stop codon-encoding sequences. AAUAAA: SV40 poly(A) tail. **E)** Western blot of IRE1α in ΔLD pool. WT IRE1α is ~100kD and ΔLD mutant is ~60kD.

REFERENCES

1. Cox, J. S., Shamu, C. E. & Walter, P. Transcriptional induction of genes encoding endoplasmic reticulum resident proteins requires a transmembrane protein kinase. *Cell* **73**, 1197–1206 (1993).
2. Mori, K., Ma, W., Gething, M. J. & Sambrook, J. A transmembrane protein with a cdc2+/CDC28-related kinase activity is required for signaling from the ER to the nucleus. *Cell* **74**, 743–756 (1993).
3. Haze, K., Yoshida, H., Yanagi, H., Yura, T. & Mori, K. Mammalian transcription factor ATF6 is synthesized as a transmembrane protein and activated by proteolysis in response to endoplasmic reticulum stress. *Mol Biol Cell* **10**, 3787–3799 (1999).
4. Harding, H. P., Zhang, Y. & Ron, D. Protein translation and folding are coupled by an endoplasmic-reticulum-resident kinase. *Nature* **397**, 271–274 (1999).
5. Hetz, C. The unfolded protein response: controlling cell fate decisions under ER stress and beyond. *Nat Rev Mol Cell Biol* **13**, 89–102 (2012).
6. Tabas, I. & Ron, D. Integrating the mechanisms of apoptosis induced by endoplasmic reticulum stress. *Nat Cell Biol* **13**, 184–190 (2011).
7. Halbleib, K. *et al.* Activation of the Unfolded Protein Response by Lipid Bilayer Stress. *Molecular Cell* **67**, 673-684.e8 (2017).
8. Cho, H. *et al.* Intrinsic Structural Features of the Human IRE1α Transmembrane Domain Sense Membrane Lipid Saturation. *Cell Reports* **27**, 307-320.e5 (2019).
9. Volmer, R., van der Ploeg, K. & Ron, D. Membrane lipid saturation activates endoplasmic reticulum unfolded protein response transducers through their transmembrane domains. *Proc Natl Acad Sci U S A* **110**, 4628–4633 (2013).
10. Rutkowski, D. T. & Hegde, R. S. Regulation of basal cellular physiology by the homeostatic unfolded protein response. *J Cell Biol* **189**, 783–794 (2010).
11. Oikawa, D., Kimata, Y., Takeuchi, M. & Kohno, K. An essential dimer-forming subregion of the endoplasmic reticulum stress sensor Ire1. *Biochem J* **391**, 135–142 (2005).
12. Amin-Wetzel, N., Neidhardt, L., Yan, Y., Mayer, M. P. & Ron, D. Unstructured regions in IRE1α specify BiP-mediated destabilisation of the luminal domain dimer and repression of the UPR. *eLife* **8**, e50793 (2019).
13. Kimata, Y. *et al.* Two regulatory steps of ER-stress sensor Ire1 involving its cluster formation and interaction with unfolded proteins. *J Cell Biol* **179**, 75–86 (2007).
14. Bertolotti, A., Zhang, Y., Hendershot, L. M., Harding, H. P. & Ron, D. Dynamic interaction of BiP and ER stress transducers in the unfolded-protein response. *Nat Cell Biol* **2**, 326–332 (2000).
15. Okamura, K., Kimata, Y., Higashio, H., Tsuru, A. & Kohno, K. Dissociation of Kar2p/BiP from an ER sensory molecule, Ire1p, triggers the unfolded protein response in yeast. *Biochem Biophys Res Commun* **279**, 445–450 (2000).

16. Papa, F. R., Zhang, C., Shokat, K. & Walter, P. Bypassing a Kinase Activity with an ATP-Competitive Drug. *Science* **302**, 1533–1537 (2003).
17. So, J.-S. Roles of Endoplasmic Reticulum Stress in Immune Responses. *Mol Cells* **41**, 705–716 (2018).
18. Lee, A.-H., Iwakoshi, N. N. & Glimcher, L. H. XBP-1 Regulates a Subset of Endoplasmic Reticulum Resident Chaperone Genes in the Unfolded Protein Response. *Mol Cell Biol* **23**, 7448–7459 (2003).
19. Yoshida, H. *et al.* A Time-Dependent Phase Shift in the Mammalian Unfolded Protein Response. *Developmental Cell* **4**, 265–271 (2003).
20. Yamamoto, K. *et al.* Human HRD1 promoter carries a functional unfolded protein response element to which XBP1 but not ATF6 directly binds. *J Biochem* **144**, 477–486 (2008).
21. Robblee, M. M. *et al.* Saturated Fatty Acids Engage an IRE1α-Dependent Pathway to Activate the NLRP3 Inflammasome in Myeloid Cells. *Cell Reports* **14**, 2611–2623 (2016).
22. Belyy, V., Zuazo-Gaztelu, I., Alamban, A., Ashkenazi, A. & Walter, P. Endoplasmic reticulum stress activates human IRE1α through reversible assembly of inactive dimers into small oligomers. *eLife* **11**, e74342 (2022).
23. Han, D. *et al.* IRE1α Kinase Activation Modes Control Alternate Endoribonuclease Outputs to Determine Divergent Cell Fates. *Cell* **138**, 562–575 (2009).
24. Hollien, J. & Weissman, J. S. Decay of Endoplasmic Reticulum-Localized mRNAs During the Unfolded Protein Response. *Science* **313**, 104–107 (2006).
25. Almanza, A. *et al.* Endoplasmic reticulum stress signalling – from basic mechanisms to clinical applications. *The FEBS Journal* **286**, 241–278 (2019).
26. Cho, N. H. *et al.* IDF Diabetes Atlas: Global estimates of diabetes prevalence for 2017 and projections for 2045. *Diabetes Research and Clinical Practice* **138**, 271–281 (2018).
27. Amen, O. M., Sarker, S. D., Ghildyal, R. & Arya, A. Endoplasmic Reticulum Stress Activates Unfolded Protein Response Signaling and Mediates Inflammation, Obesity, and Cardiac Dysfunction: Therapeutic and Molecular Approach. *Frontiers in Pharmacology* **10**, (2019).
28. Back, S. H. & Kaufman, R. J. Endoplasmic Reticulum Stress and Type 2 Diabetes. *Annual Review of Biochemistry* **81**, 767–793 (2012).
29. Petersen, M. C. & Shulman, G. I. Mechanisms of Insulin Action and Insulin Resistance. *Physiological Reviews* **98**, 2133–2223 (2018).
30. Özcan, U. *et al.* Chemical Chaperones Reduce ER Stress and Restore Glucose Homeostasis in a Mouse Model of Type 2 Diabetes. *Science* **313**, 1137–1140 (2006).
31. Özcan, U. *et al.* Endoplasmic Reticulum Stress Links Obesity, Insulin Action, and Type 2 Diabetes. *Science* **306**, 457–461 (2004).

32. Eletto, D., Eletto, D., Boyle, S. & Argon, Y. PDIA6 regulates insulin secretion by selectively inhibiting the RIDD activity of IRE1. *FASEB J* **30**, 653–665 (2016).

33. Lipson, K. L., Ghosh, R. & Urano, F. The Role of IRE1α in the Degradation of Insulin mRNA in Pancreatic β-Cells. *PLoS One* **3**, e1648 (2008).

34. Lee, H. *et al.* Beta Cell Dedifferentiation Induced by IRE1α Deletion Prevents Type 1 Diabetes. *Cell Metab* **31**, 822-836.e5 (2020).

35. Morita, S. *et al.* Targeting ABL-IRE1α Signaling Spares ER-Stressed Pancreatic β Cells to Reverse Autoimmune Diabetes. *Cell Metab* **25**, 883-897.e8 (2017).

36. Clee, S. M., Nadler, S. T. & Attie, A. D. Genetic and Genomic Studies of the BTBR ob/ob Mouse Model of Type 2 Diabetes. *American Journal of Therapeutics* **12**, 491 (2005).

37. Harrington, P. E. *et al.* Unfolded Protein Response in Cancer: IRE1α Inhibition by Selective Kinase Ligands Does Not Impair Tumor Cell Viability. *ACS Med. Chem. Lett.* **6**, 68–72 (2015).

38. Ghosh, R. *et al.* Allosteric inhibition of the IRE1α RNase preserves cell viability and function during endoplasmic reticulum stress. *Cell* **158**, 534–548 (2014).

39. Colon-Negron, K. A. & Papa, F. R. Pharmacological Targeting of IRE1α Ameliorates Insulin Resistance Through Preservation of the Insulin Receptor Signaling Pathway. (University of California San Fancisco).

40. Lan, H. *et al.* Gene Expression Profiles of Nondiabetic and Diabetic Obese Mice Suggest a Role of Hepatic Lipogenic Capacity in Diabetes Susceptibility. *Diabetes* **52**, 688–700 (2003).

41. Captisol. https://www.captisol.com/.

42. Grote, C. W. *et al.* Peripheral nervous system insulin resistance in ob/ob mice. *Acta Neuropathologica Communications* **1**, 15 (2013).

43. Howard, B. V. Insulin resistance and lipid metabolism. *The American Journal of Cardiology* **84**, 28–32 (1999).

44. Hudkins, K. L. *et al.* BTBR Ob/Ob mutant mice model progressive diabetic nephropathy. *J Am Soc Nephrol* **21**, 1533–1542 (2010).

45. Kim, K. E. *et al.* Caloric restriction of db/db mice reverts hepatic steatosis and body weight with divergent hepatic metabolism. *Sci Rep* **6**, 30111 (2016).

46. Mahendran, Y. *et al.* Association of Ketone Body Levels With Hyperglycemia and Type 2 Diabetes in 9,398 Finnish Men. *Diabetes* **62**, 3618–3626 (2013).

47. Tirosh, A. *et al.* Changes in triglyceride levels over time and risk of type 2 diabetes in young men. *Diabetes Care* **31**, 2032–2037 (2008).

48. DeFronzo, R. A., Bonadonna, R. C. & Ferrannini, E. Pathogenesis of NIDDM. A balanced overview. *Diabetes Care* **15**, 318–368 (1992).

49. Teodoro-Morrison, T., Schuiki, I., Zhang, L., Belsham, D. D. & Volchuk, A. GRP78 overproduction in pancreatic beta cells protects against high-fat-diet-induced diabetes in mice. *Diabetologia* **56**, 1057–1067 (2013).

50. Ye, R. *et al.* Grp78 heterozygosity promotes adaptive unfolded protein response and attenuates diet-induced obesity and insulin resistance. *Diabetes* **59**, 6–16 (2010).

51. Ozawa, K. *et al.* The endoplasmic reticulum chaperone improves insulin resistance in type 2 diabetes. *Diabetes* **54**, 657–663 (2005).

52. Chung, J. *et al.* HSP72 protects against obesity-induced insulin resistance. *Proceedings of the National Academy of Sciences* **105**, 1739–1744 (2008).

53. Adaptation to constant light requires Fic-mediated AMPylation of BiP to protect against reversible photoreceptor degeneration | eLife. https://elifesciences.org/articles/38752.

54. Perera, L. A. *et al.* An oligomeric state-dependent switch in the ER enzyme FICD regulates AMPylation and deAMPylation of BiP. *The EMBO Journal* **38**, e102177 (2019).

55. Casey, A. K. *et al.* Fic-mediated AMPylation tempers the unfolded protein response during physiological stress. *Proceedings of the National Academy of Sciences* **119**, e2208317119 (2022).

56. Feder, J. H., Rossi, J. M., Solomon, J., Solomon, N. & Lindquist, S. The consequences of expressing hsp70 in Drosophila cells at normal temperatures. *Genes Dev.* **6**, 1402–1413 (1992).

57. Elefant, F. & Palter, K. B. Tissue-specific Expression of Dominant Negative Mutant Drosophila HSC70 Causes Developmental Defects and Lethality. *Mol Biol Cell* **10**, 2101–2117 (1999).

58. Nylandsted, J. *et al.* Selective depletion of heat shock protein 70 (Hsp70) activates a tumor-specific death program that is independent of caspases and bypasses Bcl-2. *Proc Natl Acad Sci U S A* **97**, 7871–7876 (2000).

59. Heat shock proteins as cellular lifeguards - PubMed. https://pubmed.ncbi.nlm.nih.gov/10480757/.

60. Madhavan, A. *et al. Pharmacologic IRE1/XBP1s Activation Promotes Systemic Adaptive Remodeling in Obesity*. http://biorxiv.org/lookup/doi/10.1101/2020.12.03.408716 (2020) doi:10.1101/2020.12.03.408716.

61. Madhavan, A. *et al.* Pharmacologic IRE1/XBP1s activation promotes systemic adaptive remodeling in obesity. *Nat Commun* **13**, 608 (2022).

62. Younossi, Z. M. *et al.* Global epidemiology of nonalcoholic fatty liver disease-Meta-analytic assessment of prevalence, incidence, and outcomes. *Hepatology* **64**, 73–84 (2016).

63. Browning, J. D. *et al.* Prevalence of hepatic steatosis in an urban population in the United States: impact of ethnicity. *Hepatology* **40**, 1387–1395 (2004).

64. Kudaravalli, P. & John, S. Nonalcoholic Fatty Liver. in *StatPearls* (StatPearls Publishing, 2023).

65. Rinella, M. E. & Sanyal, A. J. Management of NAFLD: a stage-based approach. *Nat Rev Gastroenterol Hepatol* **13**, 196–205 (2016).

66. Nakagawa, H. *et al.* ER stress cooperates with hypernutrition to trigger TNF-dependent spontaneous HCC development. *Cancer Cell* **26**, 331–343 (2014).

67. Lebeaupin, C. *et al.* Endoplasmic reticulum stress signalling and the pathogenesis of non-alcoholic fatty liver disease. *J Hepatol* **69**, 927–947 (2018).

68. Vonderlin, J., Chavakis, T., Sieweke, M. & Tacke, F. The Multifaceted Roles of Macrophages in NAFLD Pathogenesis. *Cellular and Molecular Gastroenterology and Hepatology* **15**, 1311–1324 (2023).

69. Huang, W. *et al.* Depletion of liver Kupffer cells prevents the development of diet-induced hepatic steatosis and insulin resistance. *Diabetes* **59**, 347–357 (2010).

70. Adams, C. J., Kopp, M. C., Larburu, N., Nowak, P. R. & Ali, M. M. U. Structure and Molecular Mechanism of ER Stress Signaling by the Unfolded Protein Response Signal Activator IRE1. *Front. Mol. Biosci.* **6**, (2019).

71. Negrin, K. A. *et al.* IL-1 signaling in obesity-induced hepatic lipogenesis and steatosis. *PLoS One* **9**, e107265 (2014).

72. Miura, K. *et al.* Toll-like receptor 9 promotes steatohepatitis by induction of interleukin-1beta in mice. *Gastroenterology* **139**, 323-334.e7 (2010).

73. Patrick, A. L., Rullo, J., Beaudin, S., Liaw, P. & Fox-Robichaud, A. E. Hepatic leukocyte recruitment in response to time-limited expression of TNF-alpha and IL-1beta. *Am J Physiol Gastrointest Liver Physiol* **293**, G663-672 (2007).

74. Wree, A. *et al.* NLRP3 inflammasome activation results in hepatocyte pyroptosis, liver inflammation, and fibrosis in mice. *Hepatology* **59**, 898–910 (2014).

75. Wree, A. *et al.* NLRP3 inflammasome activation is required for fibrosis development in NAFLD. *J Mol Med (Berl)* **92**, 1069–1082 (2014).

76. Kaufmann, B. *et al.* Cell-specific Deletion of NLRP3 Inflammasome Identifies Myeloid Cells as Key Drivers of Liver Inflammation and Fibrosis in Murine Steatohepatitis. *Cell Mol Gastroenterol Hepatol* **14**, 751–767 (2022).

77. Manco, R. & Itzkovitz, S. Liver zonation. *Journal of Hepatology* **74**, 466–468 (2021).

78. Steinman, J. B., Salomao, M. A. & Pajvani, U. B. Zonation in NASH – A key paradigm for understanding pathophysiology and clinical outcomes. *Liver International* **41**, 2534–2546 (2021).

79. Van Campenhout, S. *et al.* Myeloid-specific IRE1alpha deletion reduces tumour development in a diabetic, non-alcoholic steatohepatitis-induced hepatocellular carcinoma mouse model. *Metabolism* **107**, 154220 (2020).

80. Kleiner, D. E. & Makhlouf, H. R. Histology of NAFLD and NASH in Adults and Children. *Clin Liver Dis* **20**, 293–312 (2016).

81. Mridha, A. R. *et al.* NLRP3 inflammasome blockade reduces liver inflammation and fibrosis in experimental NASH in mice. *Journal of Hepatology* **66**, 1037–1046 (2017).

82. Yang, G., Lee, H. E. & Lee, J. Y. A pharmacological inhibitor of NLRP3 inflammasome prevents non-alcoholic fatty liver disease in a mouse model induced by high fat diet. *Sci Rep* **6**, 24399 (2016).

83. Wei, W. *et al.* Organism-wide, cell-type-specific secretome mapping of exercise training in mice. *Cell Metabolism* **35**, 1261-1279.e11 (2023).

84. Liu, Z. *et al.* Fate Mapping via Ms4a3-Expression History Traces Monocyte-Derived Cells. *Cell* **178**, 1509-1525.e19 (2019).

85. Colino, C. I., Lanao, J. M. & Gutierrez-Millan, C. Targeting of Hepatic Macrophages by Therapeutic Nanoparticles. *Frontiers in Immunology* **11**, (2020).

86. Wu, J. H. Y., Micha, R. & Mozaffarian, D. Dietary fats and cardiometabolic disease: mechanisms and effects on risk factors and outcomes. *Nature Reviews Cardiology* **16**, 581–601 (2019).

87. Kaufman Tina M. *et al.* Application of PCSK9 Inhibitors in Practice. *Circulation Research* **124**, 32–37 (2019).

88. Davis, H. R., Compton, D. S., Hoos, L. & Tetzloff, G. Ezetimibe, a Potent Cholesterol Absorption Inhibitor, Inhibits the Development of Atherosclerosis in ApoE Knockout Mice. *Arteriosclerosis, Thrombosis, and Vascular Biology* **21**, 2032–2038 (2001).

89. Almeida, S. O. & Budoff, M. Effect of statins on atherosclerotic plaque. *Trends Cardiovasc Med* **29**, 451–455 (2019).

90. Libby, P. Interleukin-1 Beta as a Target for Atherosclerosis Therapy: The Biological Basis of CANTOS and Beyond. *J Am Coll Cardiol* **70**, 2278–2289 (2017).

91. Ridker, P. M. *et al.* Antiinflammatory Therapy with Canakinumab for Atherosclerotic Disease. *N Engl J Med* **377**, 1119–1131 (2017).

92. Bennett, M. R., Sinha, S. & Owens, G. K. Vascular smooth muscle cells in atherosclerosis. *Circ Res* **118**, 692–702 (2016).

93. Fatkhullina, A. R., Peshkova, I. O. & Koltsova, E. K. The Role of Cytokines in the Development of Atherosclerosis. *Biochemistry (Mosc)* **81**, 1358–1370 (2016).

94. Yu, X.-H., Fu, Y.-C., Zhang, D.-W., Yin, K. & Tang, C.-K. Foam cells in atherosclerosis. *Clinica Chimica Acta* **424**, 245–252 (2013).

95. Zhou, A. X. & Tabas, I. The UPR in atherosclerosis. *Semin Immunopathol* **35**, 321–332 (2013).

96. Erbay, E. *et al.* Reducing endoplasmic reticulum stress through a macrophage lipid chaperone alleviates atherosclerosis. *Nat Med* **15**, 1383–1391 (2009).

97. Intercepting IRE1 kinase-FMRP signaling prevents atherosclerosis progression. *EMBO Molecular Medicine* **14**, e15344 (2022).

98. Tufanli, O. *et al.* Targeting IRE1 with small molecules counteracts progression of atherosclerosis. *Proceedings of the National Academy of Sciences* **114**, E1395–E1404 (2017).

99. Sukhovershin, R. A., Toledano Furman, N. E., Tasciotti, E. & Trachtenberg, B. H. Local Inhibition of Macrophage and Smooth Muscle Cell Proliferation to Suppress Plaque Progression. *Methodist Debakey Cardiovasc J* **12**, 141–145 (2016).

100. Willemsen, L. & Winther, M. P. de. Macrophage subsets in atherosclerosis as defined by single-cell technologies. *The Journal of Pathology* **250**, 705–714 (2020).

101. Eun, S. Y., Ko, Y. S., Park, S. W., Chang, K. C. & Kim, H. J. IL-1β enhances vascular smooth muscle cell proliferation and migration via P2Y2 receptor-mediated RAGE expression and HMGB1 release. *Vascul Pharmacol* **72**, 108–117 (2015).

102. Parry, G. C., Martin, T., Felts, K. A. & Cobb, R. R. IL-1beta-induced monocyte chemoattractant protein-1 gene expression in endothelial cells is blocked by proteasome inhibitors. *Arterioscler Thromb Vasc Biol* **18**, 934–940 (1998).

103. Kihara, T. *et al.* Interleukin-1β enhances cell adhesion in human endothelial cells via microRNA-1914–5p suppression. *Biochemistry and Biophysics Reports* **27**, 101046 (2021).

104. Hetz, C. & Glimcher, L. H. Fine-tuning of the unfolded protein response: Assembling the IRE1alpha interactome. *Mol Cell* **35**, 551–561 (2009).

105. Hetz, C. & Papa, F. R. The Unfolded Protein Response and Cell Fate Control. *Molecular Cell* **69**, 169–181 (2018).

106. Chen, Y. & Brandizzi, F. AtIRE1A/AtIRE1B and AGB1 independently control two essential unfolded protein response pathways in Arabidopsis. *Plant J* **69**, 266–277 (2012).

107. Wang, L. *et al.* Metabolic Interactions between the Lands Cycle and the Kennedy Pathway of Glycerolipid Synthesis in Arabidopsis Developing Seeds[W]. *Plant Cell* **24**, 4652–4669 (2012).

108. Zhou, J. *et al.* The crystal structure of human IRE1 luminal domain reveals a conserved dimerization interface required for activation of the unfolded protein response. *Proc Natl Acad Sci U S A* **103**, 14343–14348 (2006).

109. Karagöz, G. E. *et al.* An unfolded protein-induced conformational switch activates mammalian IRE1. *eLife* **6**, e30700 (2017).

110. Li, H., Korennykh, A. V., Behrman, S. L. & Walter, P. Mammalian endoplasmic reticulum stress sensor IRE1 signals by dynamic clustering. *Proceedings of the National Academy of Sciences* **107**, 16113–16118 (2010).

111. Promlek, T. *et al.* Membrane aberrancy and unfolded proteins activate the endoplasmic reticulum stress sensor Ire1 in different ways. *MBoC* **22**, 3520–3532 (2011).

112. Ferri, E. *et al.* Activation of the IRE1 RNase through remodeling of the kinase front pocket by ATP-competitive ligands. *Nat Commun* **11**, 6387 (2020).

113. Covarrubias, S. *et al.* CRISPR/Cas-based screening of long non-coding RNAs (lncRNAs) in macrophages with an NF-κB reporter. *J Biol Chem* **292**, 20911–20920 (2017).